UNIVERSIDAD DE LA LAGUNA
FACULTAD DE CIENCIAS. SECCIÓN DE FÍSICA

MÁSTER EN ASTROFÍSICA

TRABAJO DE FIN DE MÁSTER

THE SOURCE OF GAS FUELLING STAR-FORMATION IN EAGLE GALAXIES

Laura Elizabeth Scholz Díaz

Tutor: **Dr. Claudio Dalla Vecchia**
Co-tutor: **Dr. Jorge Sánchez Almeida**

CURSO ACADÉMICO 2019/2020

Contents

Abstract

Cosmological gas accretion is expected to play a fundamental role to fuel the star formation in galaxies from a theoretical point of view. However, observational evidence of this process remains immensely elusive and its signatures are rather indirect. Metal-poor gas accretion has been proposed to account for the observed local $Z_g - SFR$ anti-correlation seen in nearby spiral galaxies, as this accreted gas could trigger star formation locally and decrease the mean metallicity of the gas. Using the state-of-the-art cosmological hydrodynamical simulation EAGLE, we analyze the source of the gas that sustains recent star formation in central galaxies at different epochs and find that although pre-existing gas in the galaxies is a major contribution to the star formation at lower and higher redshifts, accreted gas contributes more at high redshift. Moreover, in some low-mass objects at $z = 0$, new stars formed from gas coming from mergers with galaxies that primarily contain gas and dark matter, correspond to a significant fraction of the galaxy mass. Furthermore, we spatially resolve the Z_g and the SFR density of the star-forming gas in disc galaxies of the simulation at $z = 0$ and find that in low-mass systems and in the outskirts of more massive galaxies there are regions with high SFR and low metallicities. We find that EAGLE galaxies exhibit a similar trend with galaxy mass to the one obtained with the observed local $Z_g - \Sigma_{SFR}$ relation for spirals from the MaNGA survey. We observe that low-mass galaxies show an anti-correlation between Z_g and Σ_{SFR}, in contrast to higher mass systems, which show a positive correlation.

Resumen

Este Trabajo de Fin de Máster aborda el papel de la acreción de gas en relación con la formación estelar en galaxias de la simulación hidrodinámica cosmológica EAGLE. En el panorama actual de la formación y evolución de galaxias se estima que la acreción de gas tiene una función fundamental desde un punto de vista teórico, aunque observacionalmente continúa siendo una cuestión bastante compleja. Por ello, la evidencia observacional de este fenómeno es más bien indirecta.

La relación fundamental de metalicidad (FMR) es un ejemplo de evidencia observacional indirecta. Esta consiste en que para una masa estelar dada, galaxias con alta formación estelar (SFR) tienen gas con baja metalicidad (Z_g). Además, esta anti-correlación también ha sido vista localmente en galaxias espirales del Universo Local, donde hay regiones en los discos de las galaxias que presentan alta SFR y baja Z_g. Una posible explicación de esta anti-correlación se basa en la acreción de gas poco metálico, que podría ser capaz de alimentar la formación estelar localmente al mismo tiempo que disminuir la metalicidad media del gas.

Por otra parte, el desarrollo de simulaciones numéricas en las últimas décadas junto con los avances observaciones en el campo de la formación y evolución de galaxias han facilitado que las simulaciones cosmológicas de vanguardia se hayan convertido en un herramienta fundamental para el estudio teórico de galaxias. En concreto, las simulaciones hidrodinámicas del proyecto EAGLE proporcionan poblaciones de galaxias realistas en volúmenes cosmológicos grandes al mismo tiempo que reproducen una gran cantidad de observables. En este trabajo se investiga el gas que mantiene la formación estelar en galaxias de EAGLE.

De esta forma, en la primera parte de este trabajo se estudia la procedencia del gas que alimenta la formación estelar reciente en galaxias centrales de EAGLE. Para ello, se identifican las partículas de gas que están formando estrellas en galaxias a un determinado desplazamiento al rojo, z. Después, se localizan estas partículas en un instante anterior, a z_{prev}, correspondiente a un *snapshot* anterior de la simulación. Se lleva a cabo este análisis en dos épocas diferentes, $z = 0$ y $z = 2.01$, ya que, teniendo en cuenta la historia cósmica de formación estelar, la formación estelar es considerablemente más activa alrededor de un desplazamiento al rojo de 2 y luego decae a tiempos menores. De esta forma, para ambos casos se seleccionan las estrellas nuevas formadas entre z_{prev} y z, que corresponden intervalos algo mayores a 1 Gyr. Una vez se ha identificado el gas que ha formado estas estrellas en un tiempo anterior, se hace una clasificación según la localización de este gas en z_{prev}, distinguiendo cinco categorías diferentes: 1. el gas que estaba gravitacionalmente ligado a la galaxia a z_{prev}; 2. el gas que no está ligado a ninguna galaxia a z_{prev}; 3. el

gas ligado a otra galaxia a z_{prev} que produjo un *minor merger*; 4. el gas ligado a otra galaxia a z_{prev} que produjo un *major merger*; 5. el gas ligado a una galaxia 'oscura' a z_{prev} que produjo un *merger*. Se define como galaxia 'oscura' a galaxias que principalmente contienen gas y materia oscura, siendo su masa estelar menor que un 5% de su masa bariónica.

Los resultados obtenidos en este análisis indican que hay una diferencia entre los procesos que mantienen la formación estelar en las galaxias a diferentes épocas. Se observa aunque el gas que ya estaba en la galaxia a z_{prev} domina la formación estelar en ambas épocas, a más alto z el gas que proviene de fuera de las galaxias tiene una mayor contribución en la formación estelar. Además, el número de galaxias que tienen estas contribuciones de gas acretado recientemente también aumenta considerablemente a mayor z. Aun así, a bajo z hay galaxias de baja masa que sufren *major mergers* o reciben gas poco metálico de galaxias 'oscuras', para las cuales la contribución en masa nueva de estrellas debido a gas acretado proveniente de estas fuentes es considerablemente alta en comparación con las galaxias de más alta masa. Además, las variación de las contribuciones de gas acretado con la masa de la galaxia es más uniforme a alto z.

En la segunda parte del trabajo se emplean galaxias centrales de disco a $z = 0$, para estudiar si la relación local entre $\mathrm{Z_g}$ y Σ_{SFR} (densidad superficial de tasa de formación estelar) presente en galaxias espirales cercanas también está presente en la simulación. Estas galaxias se seleccionan en la simulación aplicando criterios ya expuestos en trabajos anteriores, que mediante la restricción de las propiedades cinemáticas y de las formas de las galaxias de EAGLE, pueden identificar sus morfologías. Una vez seleccionada la muestra, se crean mapas proyectados de $\mathrm{Z_g}$ y de Σ_{SFR}. A continuación, estos mapas se utilizan para caracterizar la relación local entre estas dos cantidades, y su dependencia con la masa estelar. Así, se separan las galaxias en intervalos equiespaciados de masa y para cada uno de ellos, se realiza una ajuste lineal al gráfico de dispersión entre $\mathrm{Z_g}$ y Σ_{SFR} de todas las galaxias que pertenecen a dicho intervalo. Se comparan las pendientes obtenidas de estos ajustes lineales para cada rango de masa estelar con los resultados observacionales de la relación local $\mathrm{Z_g} - \Sigma_{\mathrm{SFR}}$.

En este segundo análisis se encuentra que en las galaxias de disco de EAGLE hay regiones de alta Σ_{SFR} y baja $\mathrm{Z_g}$, que son más apreciables en galaxias de baja masa y en las partes exteriores de galaxias de alta masa. De esta forma, se observa que galaxias de baja masa tienen pendientes negativas, y por tanto una anti-correlación entre estas cantidades, mientras que al aumentar la masa estelar la pendiente también se incrememnta hasta que para las masas más altas cambia el signo y se vuelve positiva, por lo que estas presentan una correlación. Además, se observa que esta tendencia con la masa estelar es similar en las galaxias de EAGLE y en observaciones recientes de la relación local $\mathrm{Z_g} - \Sigma_{\mathrm{SFR}}$ obtenida para galaxias espirales del Universo Local.

Chapter 1

Introduction

Numerical simulations predict that cosmological metal-poor gas accretion drives the growth of disc galaxies (e.g. Dekel & Birnboim, 2006; Dekel et al., 2009; Silk & Mamon, 2012; Genel et al., 2012). Cosmological simulations indicate that the gas that falls into galaxies and feeds the star formation corresponds to cold gas accretion (e.g. Kereš et al., 2005; Dekel et al., 2009; van de Voort et al., 2011). This 'cold mode' is expected to supply gas mainly in the form of cold filamentary streams from the cosmic web (e.g. Dekel et al., 2009; Silk & Mamon, 2012), which are able to cool rapidly and reach the galaxy disk directly to fuel star formation (e.g. Brooks et al., 2009). In this simple picture, this gas accretion mode dominates at early times and low halo masses, below $\sim 10^{12}$ $M_{\odot}$ (e.g. Birnboim & Dekel, 2003; van de Voort et al., 2011), in contrast to the 'hot mode', dominant for higher mass haloes, in which the gas falling into the halo is shock-heated to approximately the halo virial temperature, before cooling (over longer timescales), condensing, and forming stars (e.g. Birnboim & Dekel, 2003; Kereš et al., 2005). Although galaxies also grow through mergers (e.g. Guo et al., 2011; Kormendy, 2013), simulations indicate that gas accreted directly from the cosmic web dominates mergers when considering galaxies in non-dense environments (e.g. Wang et al., 2011; L'Huillier et al., 2012; Combes, 2013; van de Voort et al., 2011). Furthermore, cold-mode gas is expected to have considerably lower metallicities than galaxy outflows driven by star formation feedback or AGN activity (van de Voort & Schaye, 2012).

Despite the observational evidence of cosmic gas accretion sustaining the star formation in galaxies of the Local Universe, the evidence is still rather indirect (for a recent review, see Sánchez Almeida, 2017). This matter remains immensely elusive from an observational point of view given the highly complicated nature of the intergalactic medium (IGM) gas, predicted to be teneous and ionized, which can get mixed with the circumgalactic medium (CGM), where there is also metal-rich recycled material being re-accreted into the galaxy. Moreover, the distinction between pure gas accretion events and gas-rich minor mergers is also difficult in observations.

An example of indirect observational evidence of gas accretion is given by the correlation between stellar mass (M_*), star formation rate (SFR), and gas-phase metallicity (Z_g). It has been found that at fixed M_*, galaxies with higher SFR show lower Z_g (Ellison et al., 2008; Mannucci et al., 2010; Lara-López et al., 2010), the so-called fundamental metallicity relation (FMR). Ellison et al. (2008) and Mannucci et al. (2010) suggest that the existence

of this observed anti-correlation between metallicity and SFR is qualitatively consistent with a scenario in which stochastic metal-poor gas accretion fuels star formation. In this way, the accretion of new metal-poor gas does not change M_*, but simultaneously triggers star formation and dilutes the gas, thus decreasing the mean metallicity of the star-forming gas. Eventually, star formation consumes the gas and stellar winds and supernova ejecta increase the gas metallicity, until new metal-poor gas is accreted and the process repeats. The explanation of the FMR within this scenario has been also probed quantitatively by several recent numerical simulations and analytic models (for more details see Sánchez Almeida et al., 2014; Sánchez Almeida, 2017). In addition, there is also observational evidence of local anti-correlations between SFR and metallicity in disc galaxies in the literature (Sánchez Almeida et al., 2013, 2015). Chemical inhomogeneities have been recently found across the discs of star-forming galaxies in the Local Universe, where regions with low gas-phase metallicity coincide with enhanced SFR (Sánchez Almeida et al., 2018; Hwang et al., 2019; Sánchez-Menguiano et al., 2019). In particular, Sánchez-Menguiano et al. (2019) found local relations between Z_g and SFR surface density for nearby star-forming spiral galaxies from the MaNGA survey (Bundy et al., 2015). In this sense, metal-poor galaxies at the low-mass end exhibit an anti-correlation, whereas it reverses for more metal-rich systems at the high-mass end.

This work aims to study the gas fuelling star formation in galaxies using the state-of-the-art cosmological numerical simulation EAGLE (Schaye et al., 2015; Crain et al., 2015). Over the last few decades, numerical cosmological simulations have become a powerful tool for improving our understanding of how galaxies form and evolve (for a recent review see Vogelsberger et al., 2020). Recent simulations are able to produce realistic galaxies and reproduce a wide range of observations mainly due to the advance of our knowledge of the physical processes that drive the growth and evolution of galaxies, the improvement of numerical methods, and the increase of computing power. In particular, cosmological hydrodynamical simulations have made remarkable progress in recent years, both large-volume simulations, e.g. EAGLE, IllustrisTNG (Pillepich et al., 2018) or HORIZON-AGN (Dubois et al., 2014), which provide statistical samples of galaxies, and zoom simulations, e.g. NIHAO (Wang et al., 2015), ASPOSTLE (Sawala et al., 2016) or LATTE/FIRE (Wetzel et al., 2016), which are able to resolve smaller scales. These simulations can reasonably reproduce galaxy populations, galaxy properties and several scaling relations of observed galaxies that were not used in the calibration process.

In this project, we use the high resolution simulation of the EAGLE suite (for more details see section 3.1). The EAGLE simulations reproduce a large number of observations, including the evolution of the galaxy stellar mass function (Furlong et al., 2015), the evolution of galaxy sizes (Furlong et al., 2017) and galaxy colours (Trayford et al., 2015). They are also able to reproduce scaling relations, such as the correlation between stellar mass and gas-phase metallicity at redshift 0 (Schaye et al., 2015), the FMR up to redshift 5 (De Rossi et al., 2017) and the relation between metallicity and size, at fixed stellar mass (Sánchez Almeida & Dalla Vecchia, 2018). Lagos et al. (2016) also found a relation between neutral gas fractions, stellar masses and present SFR. While these scaling relations are formulated in terms of integrated galaxy quantities, the study of local relations between physical properties in galaxies can provide further insight into galaxy evolution. For instance, Trayford & Schaye (2019) also found the mass-metallicity relation locally, employing spatially resolved regions in galaxies. In this way, one of the

main goals of this project is to investigate whether the observed local relations between gas-phase metallicity and star formation rate are also present in EAGLE galaxies as it may bring light to how galaxies get their gas to fuel star formation.

Chapter 2

Objectives

The aim of this work is to explore the role of gas accretion in fuelling the star formation in galaxies from the EAGLE suite. We will characterize the source of the gas that fuels star formation in these galaxies and will also investigate whether the observed local relation between gas-phase metallicity and star formation rate surface density seen in the literature is also predicted by the simulation. Specifically, this project has the following objectives:

- Get acquainted with the current paradigm of how galaxies form and evolve.
- Get familiar with the EAGLE simulations, and EAGLE database.
- Derive the relative contribution of gas accretion and galaxy mergers to the star formation in EAGLE galaxies.
- Spatially resolve the Z_g and Σ_{SFR} of the star-forming gas in disc galaxies to study local relations between these quantities.
- Compare the results with observations of the resolved FMR.

Chapter 3

Methodology

In this chapter, we outline the data and methods employed in the project. In section 3.1 we give an overview of the EAGLE simulation suite, its snapshots and its database. In section 3.2 we describe the sample selection and the approaches that we follow to achieve the aforementioned objectives, whose results are shown in sections 4.1 and 4.2.

3.1 The EAGLE simulation

The Evolution and Assembly of GaLaxies and their Environments (EAGLE) project (Schaye et al., 2015; Crain et al., 2015) consists of a suite of cosmological hydrodynamical simulations conducted by the VIRGO consortium and is aimed to comprehend the formation and evolution of galaxies. These simulations were performed using a modified version of the N-body Tree-Particle-Mesh (TreePM) smoothed particle hydrodynamics (SPH) code GADGET-3, which is based on the GADGET-2 code and was last described by Springel (2005). The main modifications of the code are the update of the formulation of the SPH, the time-stepping criteria, and the implementation of a large number of subgrid routines that account for physical processes occurring on scales below the resolution limit of the simulations (such as radiative cooling, star formation, stellar evolution, metal enrichment, black hole growth and mergers, and feedback from stars and accreting black holes). These subgrid recipes are described in detail by Crain et al. (2015) and references therein.

The EAGLE simulations adopt a flat ΛCDM cosmology with parameters derived from the Planck mission data (Planck Collaboration et al., 2014) ($\Omega_m = 0.307$, $\Omega_\Lambda = 0.693$, $\Omega_b = 0.04825$, $h = 0.6777$, $\sigma_8 = 0.8288$, $n_s = 0.9611$, $Y = 0.248$) and track the evolution of baryonic and non-baryonic matter from $z = 127$ to present day. Simulations were run in periodic cubic volumes with side lengths of $L = 12$, 25, 50 and 100 comoving megaparsecs (cMpc) and are referred to as 'high resolution' or 'intermediate resolution' depending on their initial baryonic particle mass (SPH mass). Some details of the main EAGLE simulations are shown in Table 3.1.

The EAGLE suite consists of independent simulations or models with varying box sizes and resolutions. In this work we use the RECAL model, which is designed to meet the calibration criteria of the REFERENCE model at higher resolution. The subgrid recipes

Name	L (cMpc)	N	m_g $M_\odot$	m_{dm} $M_\odot$	ϵ_{comp} (ckpc)	ϵ_{prop} (pkpc)
RefL0025N0376	25	2×376^3	1.81×10^6	9.70×10^6	2.66	0.70
RecalL0025N0752	25	2×752^3	2.26×10^5	1.21×10^6	1.33	0.35
RefL0050N0752	50	2×752^3	1.81×10^6	9.70×10^6	2.66	0.70
RefL0100N1504	100	2×1504^3	1.81×10^6	9.70×10^6	2.66	0.70

Table 3.1: Characteristics of the main EAGLE simulations. From left-to-right: simulation name; comoving box size, L; number of particles, N; initial baryonic particle mass, m_g; dark matter particle mass, m_{dm}; comoving Plummer equivalent gravitational softening length, ϵ_{comp}; maximum proper softening length, ϵ_{prop}.

of the REFERENCE model are calibrated to reproduce a limited subset of observations of galaxies at $z \sim 0$, namely the galaxy stellar mass function, galaxy sizes, and the stellar mass - black hole mass relation. In this way, the RECAL model incorporates relatively small changes in the subgrid parameters compared to the default 'intermediate resolution' runs of the REFERENCE models due to its higher resolution. We use the simulation RecalL0025N0752, which has a length of 25 cMpc per side and initially has 2×752^3 particles (dark matter and gas). The initial baryonic particle mass is $m_g = 2.26 \times 10^5$ $M_\odot$ and the maximum gravitational softening length is $\epsilon_{prop} = 0.35$ pkpc, which is used to avoid singularities in the gravitational potential below this scale.

3.1.1 Particle data and EAGLE snapshots

The simulation tracks the evolution of different particle types, gas, dark matter, stars and black holes. Particle data are organised in datasets within particle type groups. All physical properties available for each particle type are described in EAGLE Team (2017) in Tables 4-7. This set of properties is different for each particle type, although there are some properties common to all types, such as position, velocity and unique particle identifier. In this project, we use the properties of gas and stars particles that are mentioned in section 3.2.

These groups and datasets are stored in snapshots written in binary HDF5 format.[1] Each snapshot corresponds to a different redshift (29 snapshots from z = 20 to present day). In addition to particle data, there are groups that contain simulation parameters, which are also described in EAGLE Team (2017).

3.1.2 Galaxy identification and EAGLE database

Each snapshot of the simulation was processed individually to locate bound structures. Dark matter haloes are identified using the Friends-of-Friends algorithm (FoF) (Davis et al., 1985) and spherical overdensity algorithms. Baryonic particles are assigned to the same halo as the nearest dark matter particle, if this particle belongs to the halo. Later, self-bound substructures within the FoF haloes are identified as galaxies or subhaloes using the SUBFIND algorithm of Springel et al. (2001); Dolag et al. (2009) using all particle

[1]Snapshots available at http://icc.dur.ac.uk/Eagle/database.php

species. A FoF halo may contain several subhaloes, thus the 'central' galaxy is defined as the subhalo at the minimum gravitational potential and the remaining galaxies as its satellites.

In order to identify the particles belonging to a FoF halo, they are tagged with a `GroupNumber`, an integer identifier of the FoF halo. Similarly, particles are tagged with a `SubGroupNumber`, an integer identifier of a subhalo within its FoF halo, so as to determine if they belong to the subhalo. Particles in a FoF halo have a `GroupNumber` that runs from 1 (first group) to N (total number of groups), and the ones that do not belong to any group have `GroupNumber`$=2^{30}$. Particles that belong to a subhalo have a `SubGroupNumber` which ranges from 0 (the 'central' galaxy of the FoF group) to N-1 (where N is the total number of subhaloes in the group), and the ones that do not belong to any subhalo have `SubGroupNumber`$=2^{30}$.

The properties of each subhalo are analyzed in post-processing so as to calculate galaxy and halo properties. At each redshift, galaxies are processed individually to produce integrated quantities from raw particle information. The post-processing steps are detailed in Schaye et al. (2015). Many properties of the haloes and galaxies can be accessed using the EAGLE database documented by McAlpine et al. (2016), which can be queried using the Structured Query Language (SQL). The database contains integrated quantities for each galaxy at each redshift, such as stellar mass, star formation rates, metallicities and luminosities, and the galaxies can be individually tracked through time using galaxy merger trees. The database for each simulation stores information in different tables, the main ones are `SubHalo, FOF, Sizes, Aperture` and `Magnitudes`. A brief description of these tables is given in Table 3.2 and their contents are detailed in Appendix B of McAlpine et al. (2016). In this work we use some galaxy properties from the `SubHalo` tables of the simulation RECALL0025N0752, which are mentioned in section 3.2, and the `Morphokinematics` table, which is described in Appendix C of Thob et al. (2019).

SQL Table Name	Contents
`SubHalo`	Main galaxy properties
`FOF`	Halo properties
`Sizes`	Galaxy sizes
`Apertures`	Galaxy properties in 3D apertures
`Magnitudes`	Galaxy photometry in the SDSS bands

Table 3.2: Main SQL tables available for each simulation.

As we mentioned before, `GroupNumber` and `SubGroupNumber` are identifiers of a FoF halo and a subhalo within a FoF halo respectively. Both properties are stored in the `SubHalo` table for each galaxy at a given redshift, so that a galaxy can be easily located using these unique identifiers. However, these are only unique to a given snapshot and hence cannot be used to identify the same halo or galaxy across multiple snapshots. Thus, each galaxy has an identifier, `GalaxyID`, also stored in the `SubHalo` table, which allows to uniquely identify a galaxy both in space and time. As we have 29 snapshots for each simulation, the 29 galaxy catalogues can be linked through time via a galaxy merger tree, so that the evolution of a galaxy can be tracked through the evolution of its `GalaxyID` with time. In order to simplify the navigation of the merger tree, the `SubHalo`

table also contains three additional properties: `TopLeafID` is the `GalaxyID` of the highest-redshift main branch progenitor, `LastProgID` is the maximum `GalaxyID` of all progenitors irrespective of their branch and `DescendentID` is the `GalaxyID` of the unique descendent galaxy of the selected galaxy. All progenitors of any galaxy at any time have an ID in the range [GalaxyID, LastProgID].

3.2 Data sample and analysis

In this project, we carry out two separate analysis to study the gas that fuels the star formation in EAGLE galaxies. The employed samples of simulated galaxies are detailed in section 3.2.1.

In the first analysis, we study the source of the gas that sustains recent star formation in simulated galaxies at different epochs. In order to do so, we trace back the gas that has recently formed stars in the galaxies and implement Python routines to match and identify particles at different times of the simulation, which are described in section 3.2.3. On the other hand, in the second one we spatially resolve the gas-phase metallicity and the star formation rate density of the star-forming gas in disc galaxies at $z = 0$ to study local relations between these two quantities and to compare them with the observed local $Z_g - \Sigma_{SFR}$ relation.

3.2.1 Sample Selection

At a given redshift, z, we use the EAGLE database to identify the galaxies of the simulation RECALL0025N0752 through their indentifiers `GalaxyID`, `GroupNumber` and `SubGroupNumber`, and to select the central galaxies (`SubGroupNumber` $= 0$) that satisfy $M_* \geq 10^8$ $M_\odot$, where M_* is the total stellar mass of the galaxy. We use this stellar mass threshold due to the resolution limit of the simulation, since smaller galaxies have too few particles for our analysis to be reliable. As mentioned in section 3.1.2, a central galaxy in a dark matter halo corresponds to the subhalo at the minimum of the gravitational potential of that halo. We also locate these galaxies at a previous redshift z_{prev} by identifying their progenitors using the merger tree properties of the database and then store their `GalaxyID`, `GroupNumber` and `SubGroupNumber`.

In our first analysis we select the galaxies according to the above criteria at two different redshifts, $z = 0$ and $z = 2.01$. We choose these epochs because the star formation is more active at $z = 2.01$ than at $z = 0$, as the cosmic star formation rate density has a peak around redshift 2 and then it declines exponentially at later times (Madau & Dickinson, 2014). Furthermore, the shape of the SFR density as a function of redshift in EAGLE is in agreement with observations (Furlong et al., 2015).

Then, for statistical purposes we also impose upper limits on the stellar mass, excluding galaxies above 10^{11} $M_\odot$ at $z = 0$ and above $10^{10.5}$ $M_\odot$ at $z = 2.01$, as we only find a central galaxy with $10^{11} < M_*\ [M_\odot] \leq 10^{11.5}$ at $z = 0$ and a single one at $z = 2.01$ with $10^{10.5} < M_*\ [M_\odot] \leq 10^{11}$. Thus, our sample at $z = 0$ consists of 417 central galaxies with M_* ranging from 10^8 to 10^{11} $M_\odot$, and analogously, the sample at $z = 2.01$ comprises

338 central galaxies with M_* between 10^8 to $10^{10.5}$ $M_\odot$. The solid lines shown in Figure 3.1 indicate the sample distributions at $z = 0$ (green) and $z = 2.01$ (red) in log-spaced stellar mass bins of 0.5 dex. Low-mass galaxies dominate both samples as galaxies with $M_* < 10^9$ $M_\odot$ correspond to 60.4% and 69.8% of the galaxies at $z = 0$ and $z = 2.01$, respectively.

On the other hand, for the second part of the project we select a subsample of central galaxies at $z = 0$ that have 'disc-like' features. In order to identify galaxy morphologies, we followed the approach described in section 3.2.2. Briefly, we use the EAGLE database to select galaxies that have a fraction of kinetic energy in ordered corotation above a certain threshold, are oblate and relatively flat. We obtain a subsample of 107 'disky' central galaxies using these constrains, which is included in Figure 3.1 as a blue dashed line. We note that there is a low number of disc galaxies with lower masses compared to the full sample at $z = 0$. This might be due to our morphological selection criteria, in which one of the constrains is based on the kinetic energy in co-rotation of the stellar component. Thus, owing to the resolution limit of the simulation, there might not be enough stellar particles in some lower mass galaxies to be able to classify them as discs according to our morphological selection criteria.

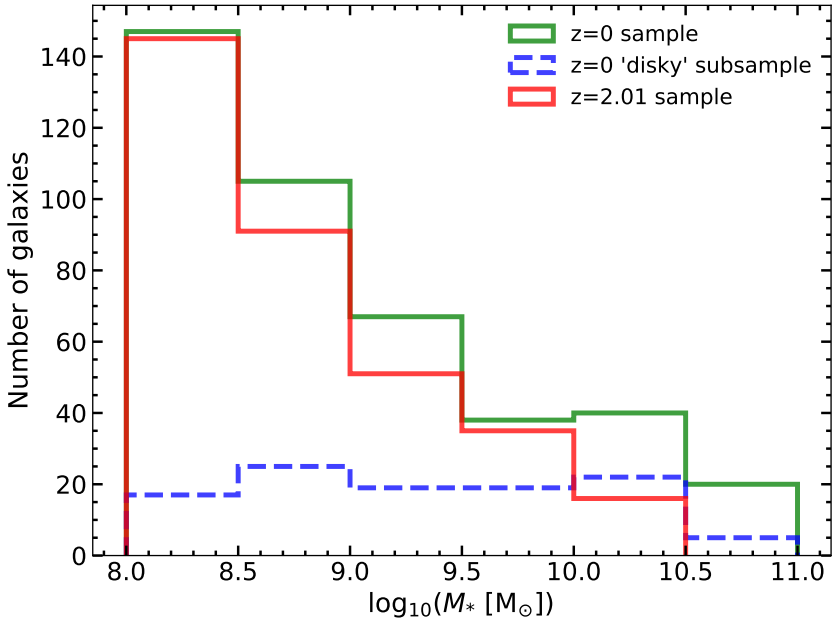

Figure 3.1: Number of galaxies as a function of the stellar mass. The green and red solid lines correspond to the samples of central galaxies at $z = 0$ with $10^8 < M_*$ [$M_\odot$] $\leq 10^{11}$, and at $z = 2.01$ with $10^8 < M_*$ [$M_\odot$] $\leq 10^{10.5}$, respectively. The blue dashed line corresponds to the subsample of central galaxies that have 'disk-like' features at $z = 0$.

Moreover, the star-forming galaxy main sequence is shown in Figure 3.2. We show the galaxy star formation rate in log-spaced stellar mass bins of 0.5 dex. The red and green solid lines indicate the median of the star formation rate of the galaxies in the samples at $z = 0$ and $z = 2.01$, respectively, in each mass bin. Analogously, the blue dashed line corresponds to the subsample of disc galaxies at $z = 0$. The colored regions correspond

to the 10$^{\text{th}}$ and 90$^{\text{th}}$ percentiles. The black solid line corresponds to the best straight-line fit to the main sequence of local galaxies in the SDSS database (Renzini & Peng, 2015). We observe that the star-forming main sequence in EAGLE at $z = 0$ is in agreement with these observations.

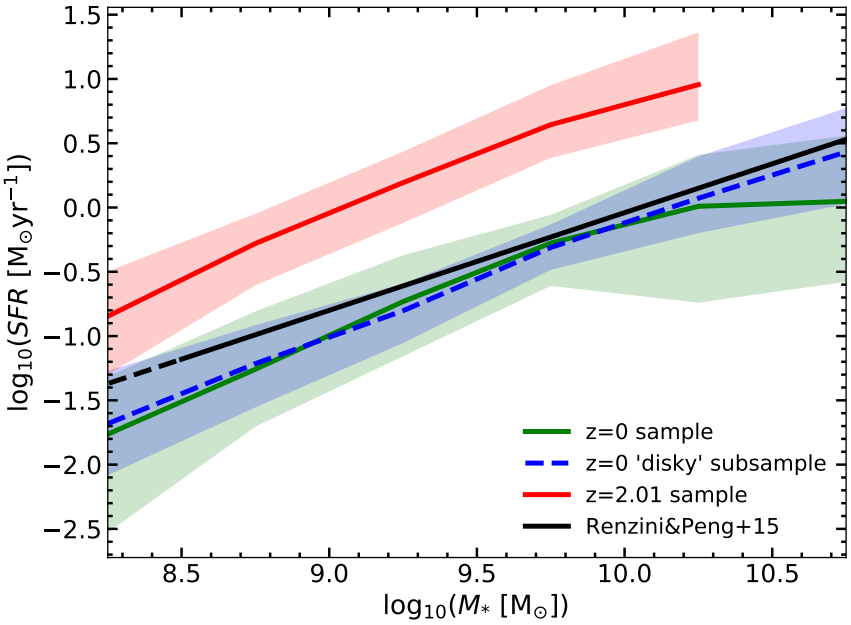

Figure 3.2: Galaxy main sequence. Star formation rate (SFR) of central galaxies in log-spaced stellar mass bins of 0.5 dex. The green and red solid lines correspond to the median SFR of the samples at $z = 0$, and at $z = 2.01$, respectively. The blue dashed line corresponds to the median SFR of the subsample of disc galaxies at $z = 0$. The colored regions indicate the 10$^{\text{th}}$ and 90$^{\text{th}}$ percentiles. The black solid line indicates the best straight-line fit to the main sequence of local galaxies in the SDSS database (Renzini & Peng, 2015) and the black dashed line corresponds to its extension to lower masses.

3.2.2 Selection of disc galaxies

In order to identify galaxies with 'disky' morphologies, we apply constrains on their kinematics and their shape parameters. First, we followed the approach described by Correa et al. (2017), who found that the morphology of EAGLE galaxies can be characterised through their rotational kinetic energy. Galaxies with $\kappa_{co} > 0.4$ correspond to 'disky' galaxies, with κ_{co} the fraction of kinetic energy, K, in ordered corotation, K_{co}^{rot}:

$$\kappa_{\rm co} = \frac{K_{\rm co}^{\rm rot}}{K} = \frac{1}{K} \sum_{i, L_{{\rm z},\vec{i}>0}} \frac{1}{2} m_i \left(\frac{L_{z,i}}{m_i R_i} \right)^2 . \tag{3.1}$$

In the above equation, m_i is the mass of each stellar particle, $L_{z,i}$ is the particle angular momentum along the direction of the total angular momentum of the stellar component of the galaxy, R_i is the projected distance to the rotation axis. The sum in Eq. (3.1) includes all co-rotating ($L_{z,i} > 0$) stellar particles within a sphere of radius equal to 30 pkpc. The total kinetic energy in the centre of mass frame is $K = \sum_i \frac{1}{2} m_i v_i^2$, again summing over all stellar particles within 30 pkpc.

Then, we also impose constrains on the galaxy shape parameters as described by Thob et al. (2019), who characterised the stellar morphologies of EAGLE galaxies by modelling the spatial distribution of their stars with an ellipsoid described by the flattening (ϵ) and triaxiality (T) parameters. These parameters are defined as:

$$\epsilon = 1 - \frac{c}{a}, \text{ and } T = \frac{a^2 - b^2}{a^2 - c^2} \tag{3.2}$$

where a, b, and c are the moduli of the major, intermediate and minor axes of the ellipsoid, respectively. They found that galaxies with $T < 0.3$ are oblate and with $\epsilon > 0.4$ are flat, both characteristics of 'disky' galaxies.

In this way, we use the EAGLE database to constrain the fraction of kinetic energy invested in corotation, the triaxiality and ellipticity of the central galaxies at $z = 0$. Thus, we select the galaxies that have $\kappa_{co} > 0.4$, are oblate ($T < 0.3$) and flat ($\epsilon > 0.4$), all in all providing a subsample of 107 'disky' galaxies.

3.2.3 Particle matching and classification analyses

In order to track the gas that has recently formed new stars in the galaxies, we implement a Python routine that analyzes two snapshots of the simulation that correspond to two different redshifts, z_{prev} and z ($z < z_{prev}$). For each galaxy at redshift z, we select the stars particles that are formed between z_{prev} and z. These stars were gas particles in z_{prev} and as particles preserve their particle identifiers (`ParticleIDs`) through time, we look for the gas particles in the previous snapshot whose particle identifiers match the ones of the selected new stars. Then, we store some properties of these gas particles such as `GroupNumber` and `SubGroupNumber`, particle identifiers, masses, star formation rates, metallicities and temperatures.

Once we have identified the gas that corresponds to newly formed stars, we implement a Python routine that makes a classification according to the location of these gas at earlier time. For each galaxy at redshift z, new stars are formed from gas particles that can be inside or outside the galaxy at redshift $z_{prev} > z$. If the particles are outside the galaxy in the previous snapshot, they are either inside another halo or are not assigned any subhalo. In this way, for each galaxy we classify the particles into five different categories by comparing the `GroupNumber` and `SubGroupNumber` of the gas particles at z_{prev} and the `GroupNumber`, `SubGroupNumber` of the progenitors galaxies. In this sense, for a given galaxy at z, new stars are formed from gas that could have come from five possible sources. These five categories are outlined in Table 3.3, and they are defined as follows: 1. the gas that was already gravitationally bound to the galaxy at z_{prev}; 2. the gas that was not bound to any subhalo at z_{prev}; 3. the gas bound to a subhalo at z_{prev} that produced a minor merger with the galaxy; 4. the gas bound to a subhalo at z_{prev} that produced a major merger with the galaxy; 5. the gas bound to a 'dark' galaxy at z_{prev} that merged with the galaxy. We define as 'dark' galaxy any subhalo in which the stellar mass is less than a five percent of its baryonic mass, i.e., they are galaxies primarily formed by gas and dark matter, with a very small contribution of stars. Minor and major mergers are identified using the stellar mass ratio of the progenitor galaxies. Mergers with mass ratios $< 1/3$ are classified as minor mergers, while those with mass ratios $\geq 1/3$ are defined as major mergers.

As mentioned in 3.2.1, we perform the previous analysis twice. For each galaxy of the sample at $z = 0$, we study the stars that are formed between $z = 0.1$ and $z = 0$, i.e, stars with ages shorter than the time interval between these two snapshots, 1.34 Gyr. Similarly, we repeat the analysis with galaxies at a higher redshift, $z = 2.01$, and we select $z_{prev} = 3.02$, in order to have similar time intervals in both analyses. Hence, we study the stars that are formed between $z = 3.02$ and $z = 2.01$, i.e., stars with ages shorter than 1.13 Gyr at that time. We note that these time intervals are typically larger than relevant time-scales for the analysis. For instance, although the gas combustion time-scale varies from 0.5 to 2 Gyr for galaxies at redshifts between 2 and 0, it is reduced by up to one order of magnitude if galaxies have intense winds (e.g. Sánchez Almeida et al., 2014). On the other hand, the time-scale in which the matter reaches the centre of the gravitational well of a halo, the free-fall time, scales with the mean density, as the rotational period of the matter around the centre of a galaxy (e.g. Binney & Tremaine, 2008). For the Milky Way, both time-scales are of the order 0.25 Gyr, and they decrease with decreasing galaxy mass. Moreover, winds, with speeds of 100 km/s, ejecting materials from star-forming regions of galaxies are common (e.g. Olmo-García et al., 2017), and the time-scale in which this material reaches the CGM is of the order of 0.2 Gyr.

CATEGORIES			DEFINITION
INSIDE THE GALAXY			Gas that was already gravitationally bound to the galaxy at the previous redshift
OUTSIDE THE GALAXY	UNBOUND		Gas that was not gravitationally bound to any subhalo at the previous redshift
	IN ANOTHER GALAXY	'DARK' GALAXY	Gas bound to a 'dark' galaxy that merged, which is a subhalo mainly formed by gas and dark matter, M_* is less than a 5% of M_{baryon}
		MINOR MERGER	Gas bound to a subhalo that produced a minor merger (with mass ratios $< 1/3$)
		MAJOR MERGER	Gas bound to a subhalo that produced a major merger (with mass ratios $\geq 1/3$)

Table 3.3: Classification according to the location of the gas particles at the previous redshift, z_{prev}. The symbol M_* is the galaxy stellar mass and M_{baryon} is the baryonic mass of the galaxy.

Moreover, we examine the variation with galaxy mass and redshift of the number of central galaxies which obtain gas to fuel recent star formation from the different categories. We separate the galaxies in log-spaced galaxy stellar mass bins of 0.5 dex. Figure 3.3 shows the number of galaxies as a function of galaxy mass. For a given category, we show the number of galaxies which formed new stars from gas coming from that category. The left panel corresponds to central galaxies at $z = 0$ with newly formed stars between $z = 0$ and $z = 0.1$ and, analogously, the right panel shows galaxies at $z = 2.01$ with stars formed between $z = 2.01$ and $z = 3.02$. Colored lines refer to the different categories defined above, i.e., the location of the gas, at $z = 0.1$ (in the left panel) and $z = 3.02$ (in the right panel). The grey line is corresponds to the total number of galaxies in each bin. At $z = 0$, all the galaxies have contributions to their recent star formation from pre-existing gas (except for two low-mass galaxies which have a $m_{new*} = 0$ in all categories, which therefore do not contribute to the analysis shown in section 4.1). Conversely, although pre-existing gas also contributes to recent star formation for all galaxies at $z = 2.01$,

accreted gas gains importance. All galaxies have also contributions to the star formation from unbound gas, and most galaxies at high redshift from gas coming from mergers with 'dark' galaxies. Generally, mergers at high redshift contribute to the recent star formation in a larger number of galaxies than at later tames. Moreover, we also see that accreted gas contributes to a larger number of galaxies at high redshift. We note that in low- and intermediate-mass galaxies at $z = 0$ we have only a few galaxies with gas contributions from mergers with 'dark' galaxies and major mergers.

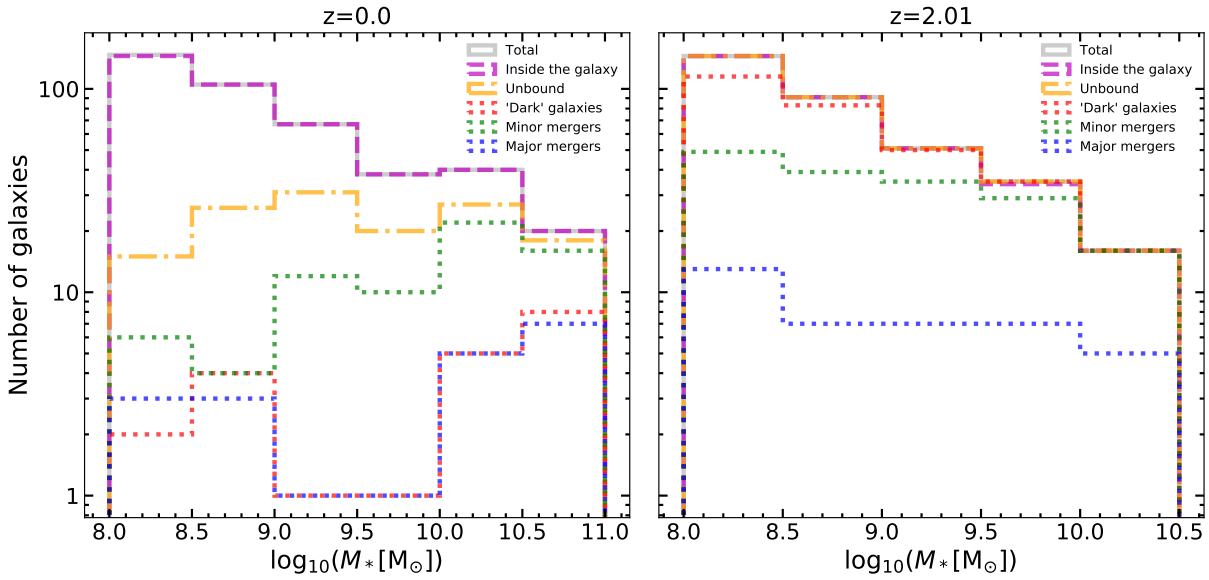

Figure 3.3: Number of central galaxies which obtain gas to fuel recent star formation from the different categories as a function of galaxy mass. For a given category, the solid line indicates the number of galaxies that formed new stars from gas belonging to that category. Left panel: centrals at $z = 0$ with the new stars formed between $z = 0.1$ and $z = 0$, i.e., stars with ages shorter than 1.34 Gyr. Right panel: centrals at $z = 2.01$ with the new stars formed between $z = 3.02$ and $z = 2.01$, i.e., stars with ages shorter than 1.13 Gyr. Colored lines refer to the location, at $z = 0.1$ (in the left panel) and $z = 2.01$ (in the right panel), of the gas that was transformed into new stars: gravitationally bound to the original galaxy (violet line), unbound (orange line), bound to a 'dark' galaxy (red), or accreted through major (blue) or minor (green) mergers (see Table 3.3). The grey line is corresponds to the total number of galaxies. Note that galaxies can qualify for more than one category if they have formed new stars from gas accreted through more than one category.

3.2.4 Maps of Z_g and Σ_{SFR} of the star-forming gas

In order to analyze the local relation between star formation rate and gas-phase metallicity in the simulation, we select the subsample of disc galaxies described in sections 3.2.1 and 3.2.2. We set them in a face-on configuration using their spin per unit mass, which is obtained from the EAGLE database. For each galaxy, we select the star-forming gas particles at the same projected distance from the center of the galaxy defined as its center of potential. For those particles, we calculate their star formation rate densities and mass-weighted average metallicities in 1×1 kpc^2 areas.

For the majority of the galaxies we select a region that contains all the star-forming gas in the subhaloes, although we note that there are a few massive galaxies which have

small substructures of star-forming gas in their haloes, that are far from the disks. These are identified by the SUBFIND algorithm as part of the galaxies due to the mass resolution limit of the simulation, as it is not possible to resolve smaller scales. In order to select the central disks of these massive galaxies, we select a region that contains more than a 95% of the mass of star-forming gas for each one of these galaxies.

Chapter 4

Results and discussion

In this chapter we describe and discuss the results obtained in this work. In section 4.1 we explore the contributions of gas accretion, galaxy mergers and pre-existing gas to the recent star formation in galaxies at two critical redshifts, 0 and 2.01. In section 4.2 we characterize the local relation between gas-phase metallicity and star formation rate in disc galaxies from EAGLE at $z = 0$. The results are compared with observations.

4.1 Gas fuelling recent SF at different epochs

In order to analyze the source of the gas that fuels recent star formation in the central galaxy samples at low and high redshifts, we follow the approach described in section 3.2.3 to trace back in time the gas particles. For each galaxy of the sample at $z = 0$, we identify the location of the gas at $z = 0.1$ that corresponds to stars formed between $z = 0.1$ and $z = 0$, i.e., stars with ages shorter than 1.34 Gyr. The new-formed stars are classified into different categories according to the location at $z = 0.1$ of the corresponding gas. Analogously, we repeat the analysis at $z = 2.01$, studying the gas that corresponds to stars that are formed between $z = 3.02$ and $z = 2.01$, i.e., stars with ages shorter than 1.13 Gyr at that time.

First, we investigate the contribution from gas that comes from different sources to the initial mass of new stars, i.e., the mass of the new stellar particles when they were born. We divide the samples in log-spaced galaxy stellar mass bins of 0.5 dex. For a given category, we compute the sum of the star particles initial masses of new-formed stars. Then, these quantities are normalized by the total initial mass in the bin. Figure 4.1 shows these initial mass fractions as a function of galaxy mass. The left panel corresponds to central galaxies at $z = 0$ with newly-formed stars between $z = 0.1$ and $z = 0$ and, analogously, the right panel shows galaxies at $z = 2.01$ with stars formed between $z = 3.02$ and $z = 2.01$. Colored lines refer to the original location of the gas that transformed into new stars: gravitationally bound to the original galaxy (violet line), unbound (orange line), bound to a 'dark' galaxy (red line), or accreted through major (blue line) or minor (green line) mergers. For a detailed description of the different categories, see section 3.2.3 and Table 3.3. The black line corresponds to the total initial mass, adding all categories, therefore, it equals one by definition. For galaxies at $z = 0$, the left panel shows that

at a given stellar mass, the contribution from stars formed from pre-existing gas in the galaxy is significantly higher than the one from stars formed from accreted gas, given that the latter corresponds to less than about 2% of the initial mass, except for high-mass galaxies. The importance of star formation due to major mergers increases in galaxies with $M_* > 10^{10.5}$ $M_\odot$ as it contribute to around 10% of the initial mass. When we look at high redshift galaxies (right panel), although stars formed from pre-existing gas in the galaxy are still dominant, the contribution from accreted gas is considerably higher than at low redshift. More than 10% of the initial mass in new stars corresponds to gas that was not bound to any galaxy, and about 10% comes from mergers with 'dark' galaxies (which primarily contain gas and dark matter). For high-mass galaxies, the contribution from minor and major mergers is higher, as in $z = 0$ galaxies. In general, the variation with stellar mass is smoother than at low redshift and the contribution from minor and major mergers clearly increases with galaxy mass.

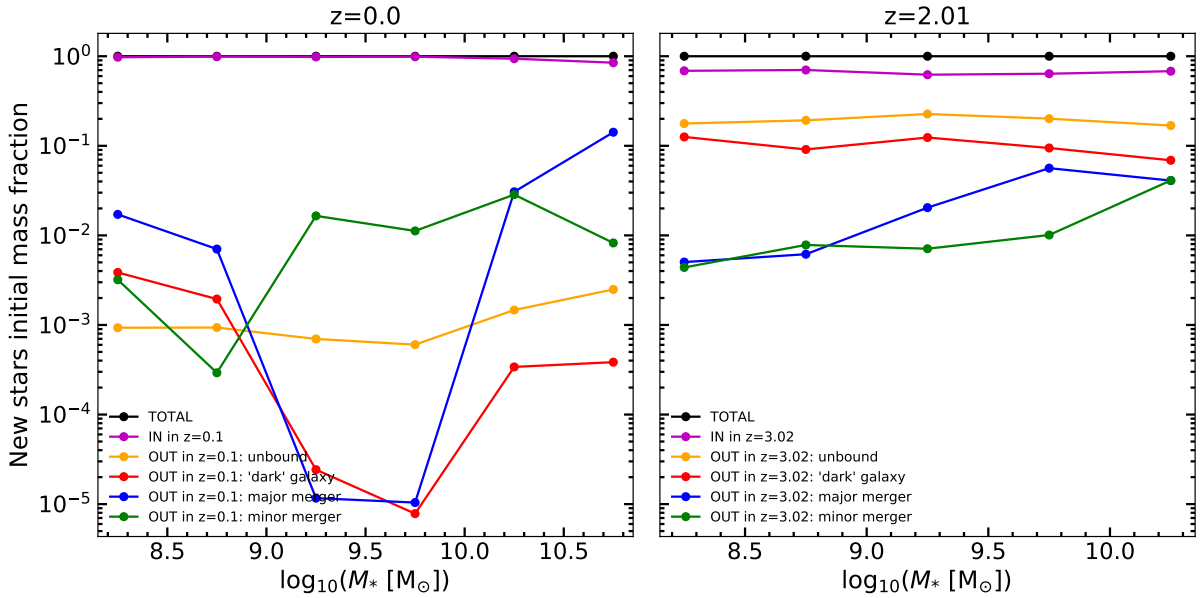

Figure 4.1: Initial mass of newly formed stars versus galaxy stellar mass, only central galaxies are considered. The galaxies are divided in log-spaced galaxy stellar mass bins of 0.5 dex. For all the galaxies in each bin, the solid lines indicate the sum of their initial masses in new stars for each category (color-coded), normalized by the total initial mass in the bin (adding all the categories). Left panel: centrals at $z = 0$ with the new stars formed between $z = 0.1$ and $z = 0$, i.e., stars with ages shorter than 1.34 Gyr. Right panel: centrals at $z = 2.01$ with the new stars formed between $z = 3.02$ and $z = 2.01$, i.e., stars with ages shorter than 1.13 Gyr. Colored lines refer to the location, at $z = 0.1$ (in the left panel) and $z = 2.01$ (in the right panel), of the gas that was transformed into new stars: gravitationally bound to the original galaxy (violet line), unbound (orange line), bound to a 'dark' galaxy (red), or accreted through major (blue) or minor (green) mergers. The black line is corresponds to the total initial mass, and equals to one.

For each galaxy, we also assess the contribution to the new stellar mass of gas coming from different sources. In this sense, for each category, we compute the mass fraction of new stars with respect to the total mass of new-formed stars (i.e., adding all the categories) for the individual galaxies. Figure 4.2 shows the mean of these mass fractions for each category, considering all the galaxies in each mass bin (including the ones that have $m_{new*} = 0$ in that category). Left and right panels correspond to the analyses at

redshifts $z = 0$ and $z = 2.01$, respectively, and the color code is the same as the one used in Figure 4.1. For each category, the solid lines correspond to the mean of the distribution and the colored regions indicate the standard deviation. We observe a similar trend as the one seen in 4.1. In the left panel of Figure 4.2 we see that, at low redshift, the major contribution to the mass in new stars is produced by pre-existing gas in the galaxy and it is considerably larger than the ones of accreted gas. Nonetheless, the contributions from accreted gas gain importance at the low- and high-mass ends. Major mergers and mergers with 'dark' galaxies have the largest contributions of accreted gas in low-mass galaxies. At higher redshifts, although pre-existing gas still dominates the recent star formation, unbound gas and gas coming from mergers with 'dark' galaxies have a considerably higher contribution than at $z = 0$ in the whole mass range.

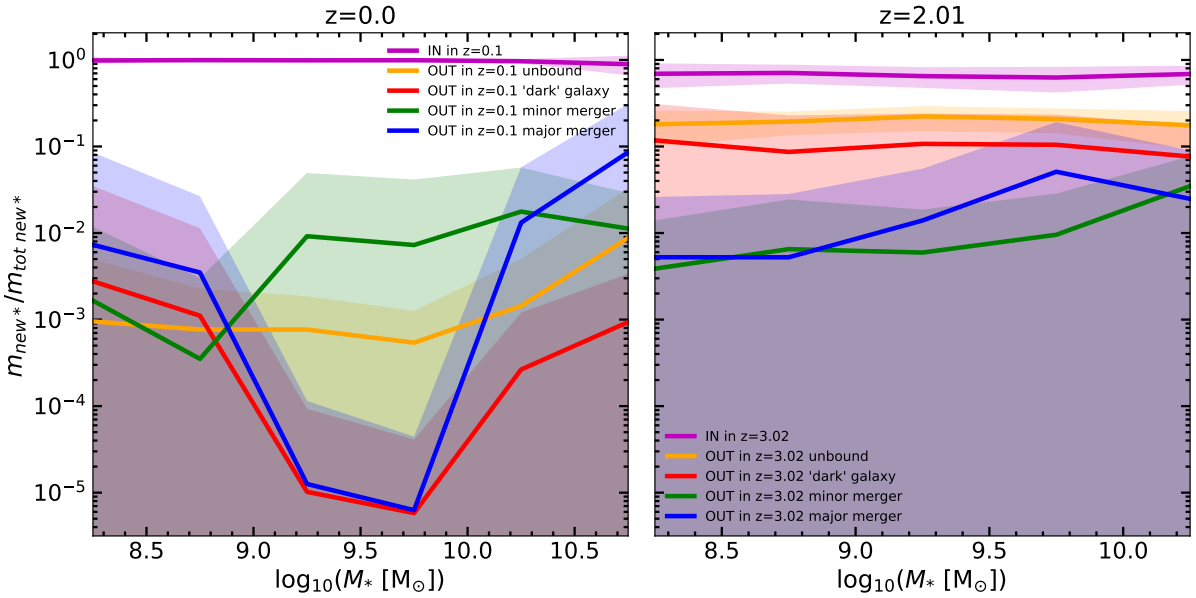

Figure 4.2: Mass fraction of new stars relative to the total mass of new stars in log-spaced stellar mass bins. For each category (color-coded), we consider all galaxies (even the ones with $m_{\rm new} = 0$). Left panel: centrals at $z = 0$ with the new stars formed between $z = 0.1$ and $z = 0$, i.e., stars with ages shorter than 1.34 Gyr. Right panel: centrals at $z = 2.01$ with the new stars formed between $z = 3.02$ and $z = 2.01$, i.e., stars with ages shorter than 1.13 Gyr. Colored lines refer to the location, at $z = 0.1$ (in the left panel) and $z = 2.01$ (in the right panel), of the gas that was transformed into new stars: gravitationally bound to the original galaxy (violet line), unbound (orange line), bound to a 'dark' galaxy (red), or accreted through major (blue) or minor (green) mergers. For each category, the solid line indicates the mean and the colored regions the standard deviation.

In addition, we also derive the relative contribution of new stellar mass with respect to the galaxy mass for individual galaxies. Figure 4.3 shows the median of these mass fractions for each category in the same mass bins as in Figure 4.1. We note that for each category we show only galaxies with newly formed stars in that category, as we see that in certain mass ranges, there are only few galaxies which contribute to some categories at $z = 0$ (see Figure 3.3). Left and right panels correspond to the analyses at redshifts $z = 0$ and $z = 2.01$, respectively, and the color code is the same as the one used in Figure 4.1. For each category, the solid line indicates the median of all the galaxies in the bin and colored region the range between the $10^{\rm th}$ and $90^{\rm th}$ percentiles. As pre-existing contributes to the

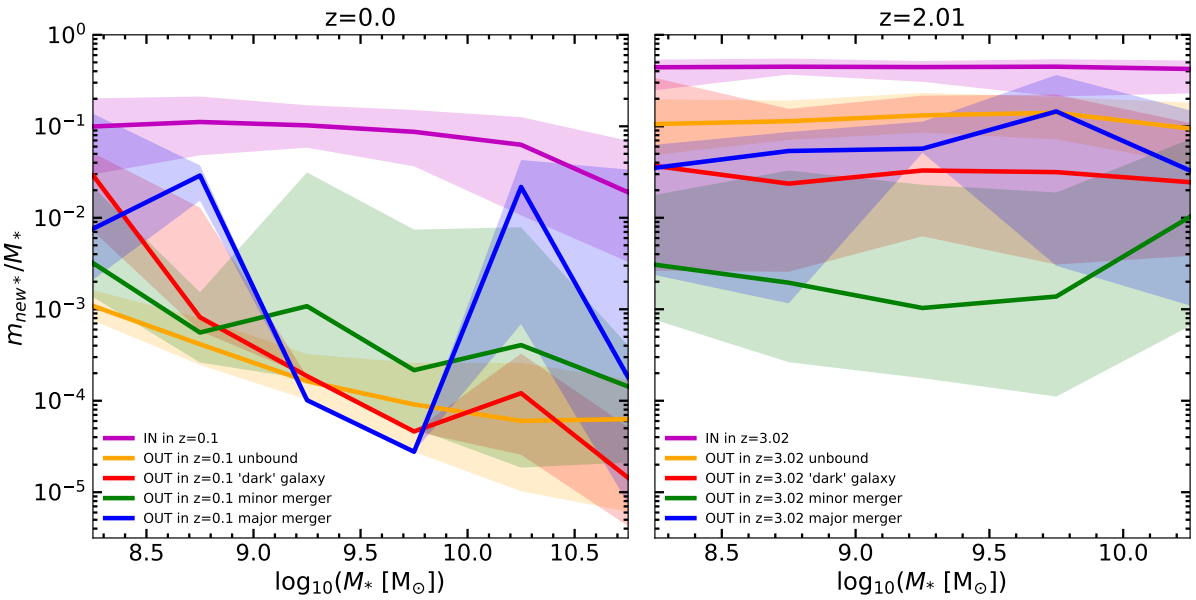

Figure 4.3: Mass fraction of new stars with respect to the total stellar mass of the galaxy in log-spaced galaxy stellar mass bins. For each category (color-coded), only galaxies with newly formed stars are considered. Left panel: centrals at $z = 0$ with the new stars formed between $z = 0.1$ and $z = 0$, i.e., stars with ages shorter than 1.34 Gyr. Right panel: centrals at $z = 2.01$ with the new stars formed between $z = 3.02$ and $z = 2.01$, i.e., stars with ages shorter than 1.13 Gyr. Colored lines refer to the location, at $z = 0.1$ (in the left panel) and $z = 2.01$ (in the right panel), of the gas that was transformed into new stars: gravitationally bound to the original galaxy (violet line), unbound (orange line), bound to a 'dark' galaxy (red), or accreted through major (blue) or minor (green) mergers. For each category, the solid line indicates the median and the colored region the 10^{th} and 90^{th} percentiles.

recent star formation in all the galaxies at $z = 0$ (see Figure 3.3), in the left panel of Figure 4.1, the dominant contribution to the stellar mass of the galaxies at present day is due to new stars formed from gas that was already bound to the galaxies at $z = 0.1$, counting for about 10% of the galaxy mass, except at the high-mass end where its contribution decreases to less than 2%. Nonetheless, star formation from accreted gas make larger mass fractions in some galaxies at the low-mass end. Indeed, given the scatter, there are low-mass galaxies with large contributions of mass in new stars produced by gas coming from mergers with 'dark' galaxies and major mergers, which are roughly comparable to the one of pre-existing gas. In contrast, in the right panel of Figure 4.1, new-formed stars contribute more to the galaxy masses in all categories than at $z = 0$, especially for the contributions of accreted gas in intermediate- and high-mass galaxies. Pre-existing, unbound gas and gas coming from mergers with 'dark' galaxies contribute to the recent star formation in most galaxies at $z = 2.01$ (see Figure 3.3). For these galaxies in the whole mass regime, new stars formed from pre-existing gas, unbound gas and gas that was in 'dark' galaxies make about 45%, 10% and roughly 3% of the galaxy mass, respectively. The large scatter in the distribution of accreted gas from 'dark' galaxies indicates that there are galaxies in which the new stars formed from this gas correspond to roughly 30% of the galaxy mass. Although there are less galaxies that have gone through mergers than galaxies with contributions from other sources of accreted gas at $z = 2.01$ (see Figure 3.3), their contributions to the galaxy mass are generally higher than at $z = 0$. We also see that the dependence with stellar mass of the fractions is smoother than at redshift 0. A

major caveat is that the statistical sample is not large, especially at redshift 0 for low and intermediate mass galaxies, where there are only a few galaxies which have contributions of gas coming from major mergers and mergers with 'dark galaxies' (see Figure 3.3).

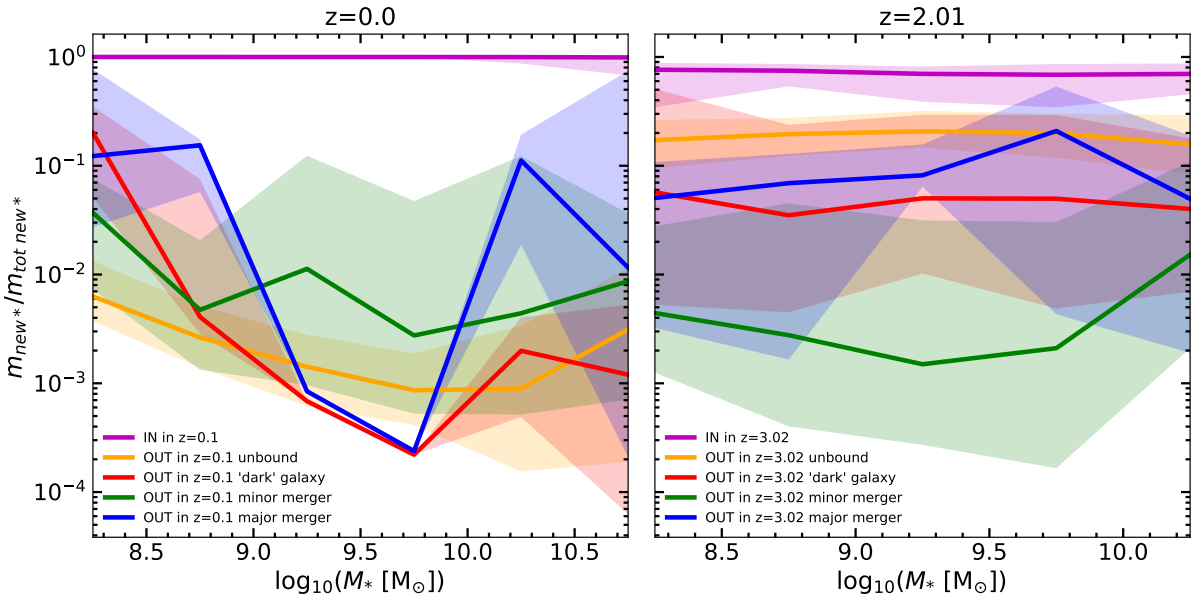

Figure 4.4: Mass fraction of new stars in a category relative to the total mass of new stars in log-spaced stellar mass bins. For each category (color-coded), only galaxies with newly formed stars are considered. Left panel: centrals at $z = 0$ with the new stars formed between $z = 0.1$ and $z = 0$, i.e., stars with ages shorter than 1.34 Gyr. Right panel: centrals at $z = 2.01$ with the new stars formed between $z = 3.02$ and $z = 2.01$, i.e., stars with ages shorter than 1.13 Gyr. Colored lines refer to the location, at $z = 0.1$ (in the left panel) and $z = 2.01$ (in the right panel), of the gas that was transformed into new stars: gravitationally bound to the original galaxy (violet line), unbound (orange line), bound to a 'dark' galaxy (red), or accreted through major (blue) or minor (green) mergers. For each category, the solid line indicates the median and the colored regions the 10^{th} and 90^{th} percentiles.

We also investigate how much does each category contribute to the total mass of new stars for each galaxy. In this case, for a given category, we calculate the fraction of new stars in each category with respect to the total mass in new stars (i.e., adding all the categories), but in contrast to Figure 4.2, we consider only galaxies with newly formed stars in that category, as in Figure 4.3. Figure 4.4 shows the median of these mass fractions as a function of galaxy mass. Left and right panels correspond to the analyses at redshifts $z = 0$ and $z = 2.01$, respectively, and the color code is the same as the one used in Figures 4.1 and 4.3. For each category, the solid line indicates the median and the colored regions the 10^{th} and 90^{th} percentiles. Despite the fact that at redshift 0 the main contribution corresponds to gas that was already in the galaxy, for the galaxies that have received gas from mergers with 'dark' galaxies and major mergers, they make about 10% of the mass in new stars at the low-mass end. Taking into account the scatter, for some galaxies that have gone through major mergers, this fraction becomes 60%, and for some galaxies that obtained gas from mergers with 'dark' galaxies it reaches a 20%. Conversely, as mentioned before, given that most galaxies have contributions from accreted gas at high redshift, the one of pre-existing gas is slightly lower, while unbound gas contributes with more than the 10% of the mass of new stars. In this sense, considering the galaxies with contributions of mergers with 'dark' galaxies (which are significantly more galaxies in the

whole mass range than at $z = 0$) and given the scatter, in some systems the fraction of new stars formed from gas coming from mergers with 'dark' galaxies becomes 40%.

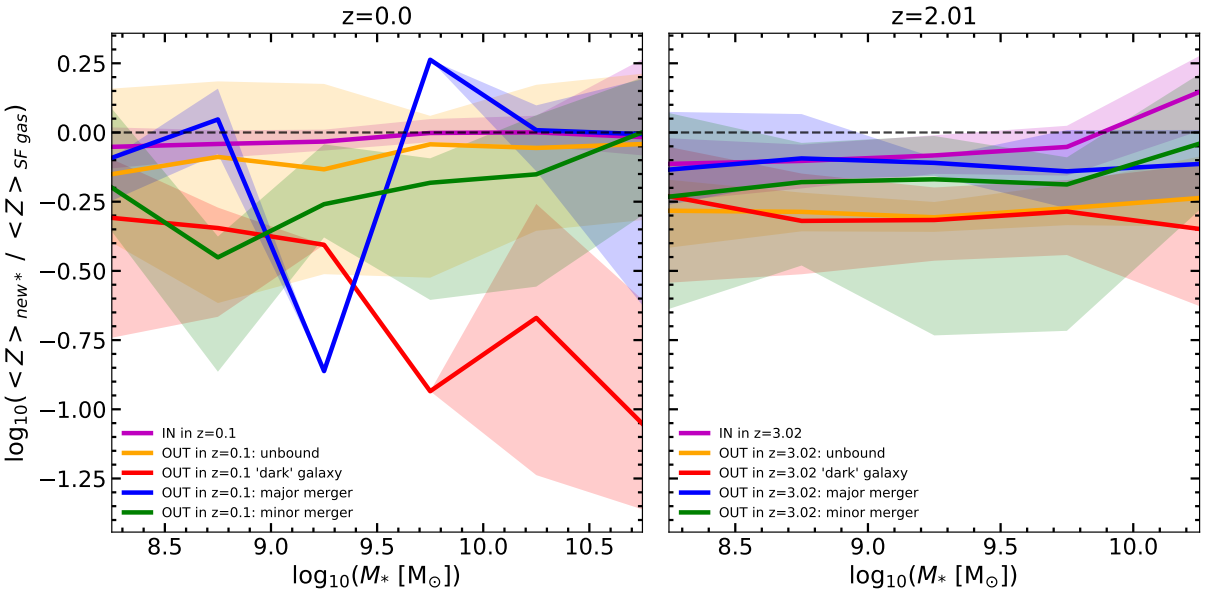

Figure 4.5: Mean metallicity of the new stars relative to the mean metallicity of the star-forming gas of the galaxy in log-spaced stellar mass bins. For each category (color-coded), only galaxies with newly formed stars are considered. Left panel: centrals at $z = 0$ with the new stars formed between $z = 0.1$ and $z = 0$, i.e., stars with ages shorter than 1.34 Gyr. Right panel: centrals at $z = 2.01$ with the new stars formed between $z = 3.02$ and $z = 2.01$, i.e., stars with ages shorter than 1.13 Gyr. Colored lines refer to the location, at $z = 0.1$ (in the left panel) and $z = 2.01$ (in the right panel), of the gas that was transformed into new stars: gravitationally bound to the original galaxy (violet line), unbound (orange line), bound to a 'dark' galaxy (red), or accreted through major (blue) or minor (green) mergers. For each category, the solid line indicates the median and the colored regions enclose the 10^{th} and 90^{th} percentiles. The black dashed line is equal to 0 and is included for reference.

We also examine how the metallicity of the new stars varies depending on the source of the gas that formed them. For each galaxy, we calculate the mean metallicity of the new stars with respect to the mean metallicity of the star-forming gas of the galaxy. Figure 4.5 shows the median of these quantities for each category and stellar mass bins. Left and right panels correspond to the analyses at redshifts $z = 0$ and $z = 2.01$, respectively, and the color code is the same as the one used in Figures 4.1, 4.3 and 4.4. For each category, the solid line indicates the median and colored area the 10^{th} and 90^{th} percentiles. At redshift 0, the metallicity of the stars formed from pre-existing gas is quite similar to the metallicity of the star-forming gas in the whole mass range, and with a scatter considerably lower than the metallicities from gas accreted to the galaxy. In contrast, the metallicity of the stars formed from gas that was previously bound to 'dark' galaxies is considerably lower than the mean metallicity of the star-forming gas. We also observe that it decreases with increasing galaxy mass for reasons which are not clear at present. The metallicity of the contribution of minor mergers is also lower, although it increases at low- and high- mass ends. The metallicity of major mergers is quite similar to the metallicity of the new stars formed from pre-existing gas, for low- and high-mass galaxies. Intermediate-mass galaxies have a behaviour quite irregular, which might be due to the fact that only few galaxies contribute to this category in this stellar mass range. The metallicities of the stars formed

from unbound gas is quite high, given that the median of the distribution is only slightly lower than the one corresponding to gas already in the galaxy, with a distribution with a very large scatter. On the other hand, at high 2.01, the metallicites of the stars formed from pre-existing gas and from gas coming from major mergers are quite similar, both slightly lower than the metallicity of the star-forming gas in the galaxies, although the former shows higher metallicities for high-mass galaxies, which might indicate that these stars are formed from recycled gas. Despite the metallicity of minor mergers is slightly lower, it also increases for high-mass galaxies. The metallicites of the stars that are formed by unbound gas or gas coming from mergers with gas-rich 'dark' galaxies are slightly lower than the one of the stars formed from pre-existing gas, and both quite similar. We also see that the variation with stellar mass is smoother at higher redshift. In low-mass galaxies, recent star formation due to gas coming from mergers with gas-rich 'dark' galaxies has a metallicity distribution that is very broad, indicating that there are galaxies whose newly formed stars have considerably lower metallicities than the metallicity of the star-forming gas.

The stars formed from unbound gas at redshift 0 have a considerably high metallicity which might indicate that this gas comes from galactic fountains, where material pre-processed in stars is ejected and then can cool in the halo and be re-accreted onto the galaxy disc. Thus, hot galactic winds are operationally classified as not gravitationally bound to the galaxy.

We see that at different epochs the processes that drive the star formation are also different. As we mentioned before, the cosmic star formation rate density peaks around redshift 2 and then it drops exponentially at lower redshifts (Madau & Dickinson, 2014). In this fashion, this is consistent with the fact that recent star formation contributes more to the mass of the simulated galaxies at $z = 2.01$ than at present day, as star formation is more active at earlier times. Furthermore, cold gas accretion is predicted to be the main mode of accretion at earlier times and in low-mass galaxies at later times (see Chapter 1). In this way, we observe in the simulation how metal-poor gas coming from mergers with 'dark' galaxies, which primarily consist in gas and dark matter, has a noticeable contribution in some low-mass galaxies at $z = 0$, while it declines for higher mass systems. Conversely, at earlier times, most of the galaxies have formed stars from gas coming from these obscure galaxies and their contribution remains more or less constant with the stellar mass.

In addition, the star formation is most efficient in haloes with masses of $\sim 10^{12}$ $M_\odot$ when we look at the stellar mass to halo mass ratio as a function of halo mass (Behroozi et al., 2013). Feedback from supernova and AGN are expected to be key processes that regulate star formation operating roughly above and below this characteristic halo mass, respectively. For galaxies in the high-mass end at later times, AGN feedback might be the cause of the reduction of new stars formed from pre-existing gas. We see that for galaxies which have gone through major mergers, the corresponding contribution tend to be more important in these massive galaxies.

4.2 Local $Z_g - \Sigma_{SFR}$ relation

In this second part of the project, we analyze the subsample of disc galaxies (see section 3.2.1) in order to study whether the local $Z_g - \Sigma_{SFR}$ relation seen in observations of nearby spiral galaxies (Sánchez-Menguiano et al., 2019) is also present in disc galaxies of the simulation and also with the aim to compare our results with this observed local relation.

EAGLE data provide spatially resolved gas-phase metallicity and star formation rate for the individual galaxies. Thus, for each galaxy we calculate the plane-of-the-sky projected star formation rate density and the mass-weighted average metallicity considering all the star-forming gas particles. The projection is made using bins of 1 kpc^2 and with the galaxy in face-on configuration. We show maps of these integrated quantities for representative galaxies of different stellar masses in Figures 4.6-4.8. The red circle has a radius equal to the physical radius of a sphere that encloses half of the stellar mass of the galaxy.

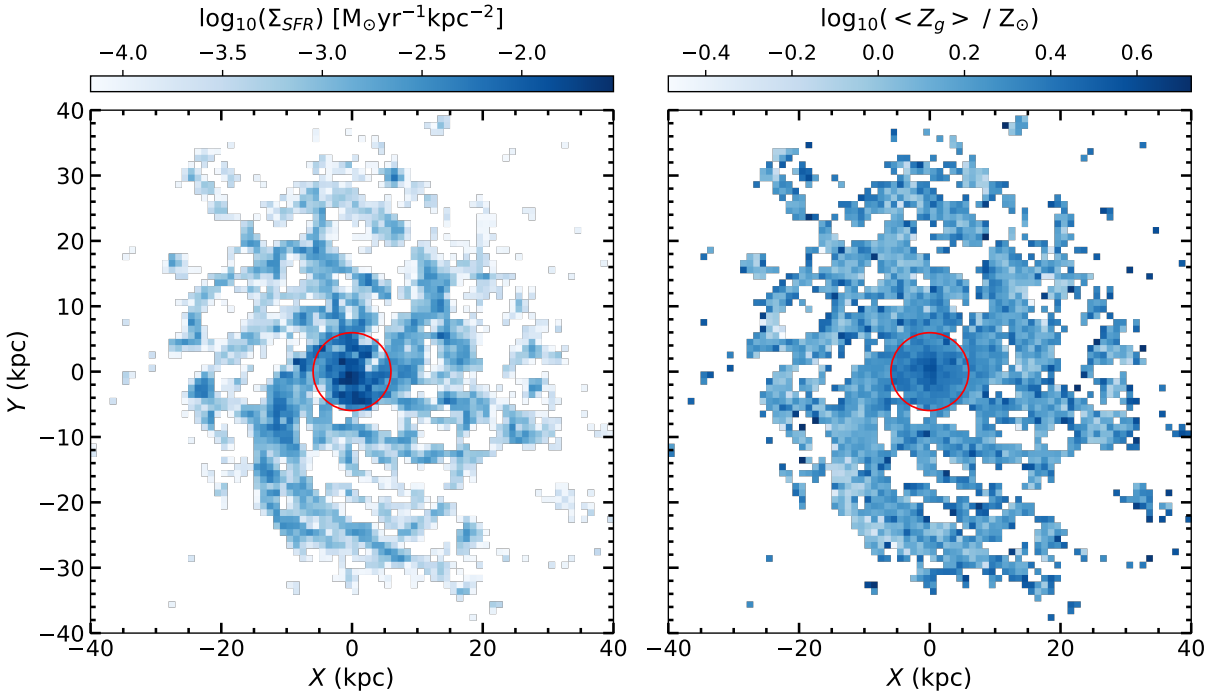

Figure 4.6: Star formation rate surface density (left panel) and mass-weighted average metallicity (right panel) for galaxy 817104 with $\log_{10}(M_*/M_\odot) = 10.27$. The red circle has a radius equal to the physical radius of a sphere that encloses half of the stellar mass of the galaxy. The central increase of SFR surface density comes with an increase of metallicity.

The example in Figure 4.6 corresponds to the high-mass end, with a stellar mass of $\sim 2 \times 10^{10}$ M$_\odot$. One observes certain regions in the outer parts of the galaxy where higher SFR coincide with lower Z_g, but the correlation reverses sign in the central parts of the galaxy where regions of higher SFR also have considerably higher metallicities. Figure 4.7 shows a galaxy with a lower stellar mass than in the previous case, $M_* \sim 5 \times 10^9$ M$_\odot$. In this galaxy, there are regions in the outskirts where the anti-correlation between Z_g and SFR is more significant than in the previous case. While in the case of a galaxy at

the low-mass end, as the one shown in Figure 4.8 with a stellar mass of $\sim 7 \times 10^8$ $M_\odot$, these two quantities are clearly more anti-correlated. In the left panel of Figure 4.8 we see how several regions with high values of SFR which in the right panel correspond to low metallicity values.

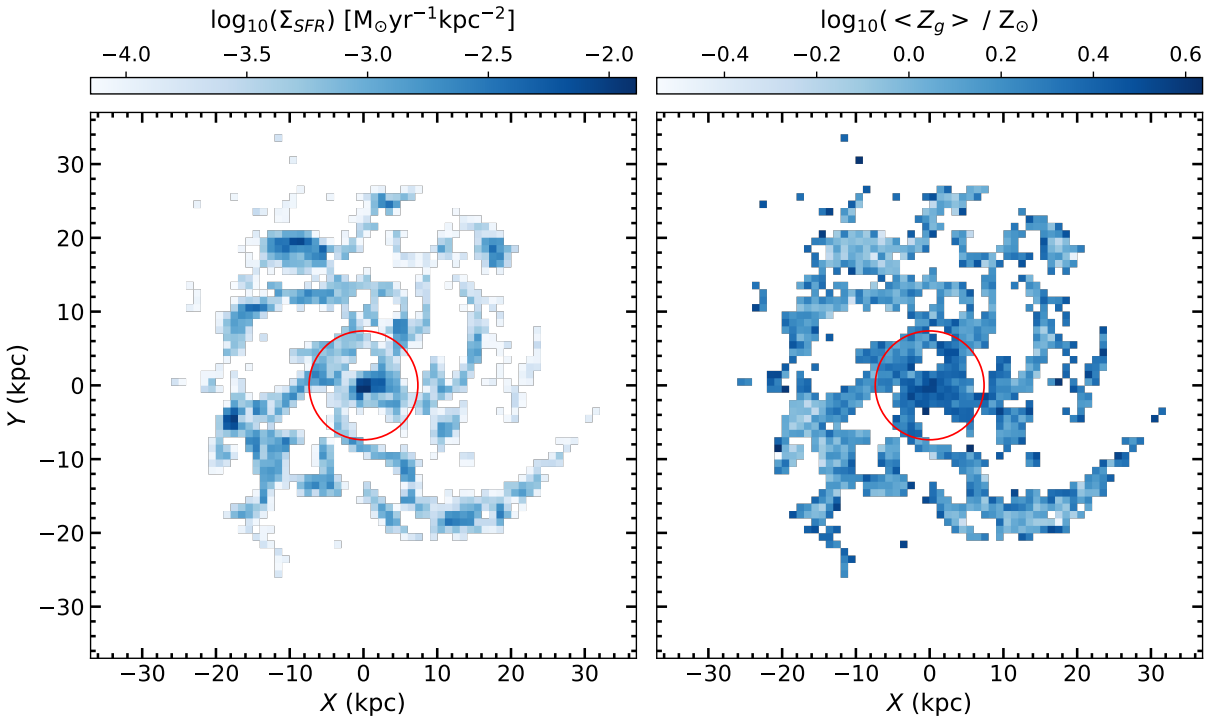

Figure 4.7: Star formation rate surface density (left panel) and mass-weighted average metallicity (right panel) for galaxy 1019529 with $\log_{10}(M_*/M_\odot) = 9.72$. The red circle has a radius equal to the physical radius of a sphere that encloses half of the stellar mass of the galaxy.

In order to quantify the relation between Z_g and Σ_{SFR}, we divide the subsample into six stellar mass bins of 0.5 dex. Then, for each bin, we perform linear fits to the scatter plot of mass-weighted average metallicity versus star formation rate surface density for all the galaxies that fall in the mass bin. Thus, the fitted points correspond to the values shown in the right and left panels of Figures 4.6-4.8. We show the slopes of these linear fits as a function of galaxy stellar mass in Figure 4.9. The error bar in the y-axis correspond to the errors of the linear fit and in the x-axis to the width of the stellar mass bin. The grey dashed straight line has a slope equal to zero and is included for reference.

We compare these findings from EAGLE with the observational results of Sánchez-Menguiano et al. (2019), who found a local relation $Z_g - \Sigma_{SFR}$ from 736 nearby spiral galaxies from the MaNGA survey. The comparison is not seamless. We have to take into account that there are differences in the way simulated and observational relations were obtained. Hence, we only attempt a qualitative comparison of the slopes of found in the simulation and in the observations, in order to see whether EAGLE galaxies show the observed trend with galaxy stellar mass.

Sánchez-Menguiano et al. (2019) obtain the local relation by spatially resolving the Z_g and SFR density in galaxy discs and then substracting the azimuthally averaged radial profile to the observed distribution. Moreover, they also showed a relation between the

slope of the local $Z_g - \Sigma_{SFR}$ relation and the galaxy stellar mass, where galaxies with higher masses have also higher slope values, and found a 2nd order polynomial fit to this relation (Table 1 of Sánchez-Menguiano et al., 2019). The fit was carried out in individual galaxies, and then the mean and standard deviation of all the galaxies in the bin were represented. We include this 2nd order polynomial fit in Figure 4.9 as a green dashed line. The green solid line corresponds this polynomial fit with a shift of -0.2 dex due to the different initial mass functions (IMF) used in the EAGLE simulation and in interpreting the observations. Sánchez-Menguiano et al. (2019) use PIPE3D (Sánchez et al., 2016) to compute stellar masses, in which the single stellar population (SSP) model spectra adopt a modified Salpeter IMF, while EAGLE uses the Chabrier IMF (Schaye et al., 2015).

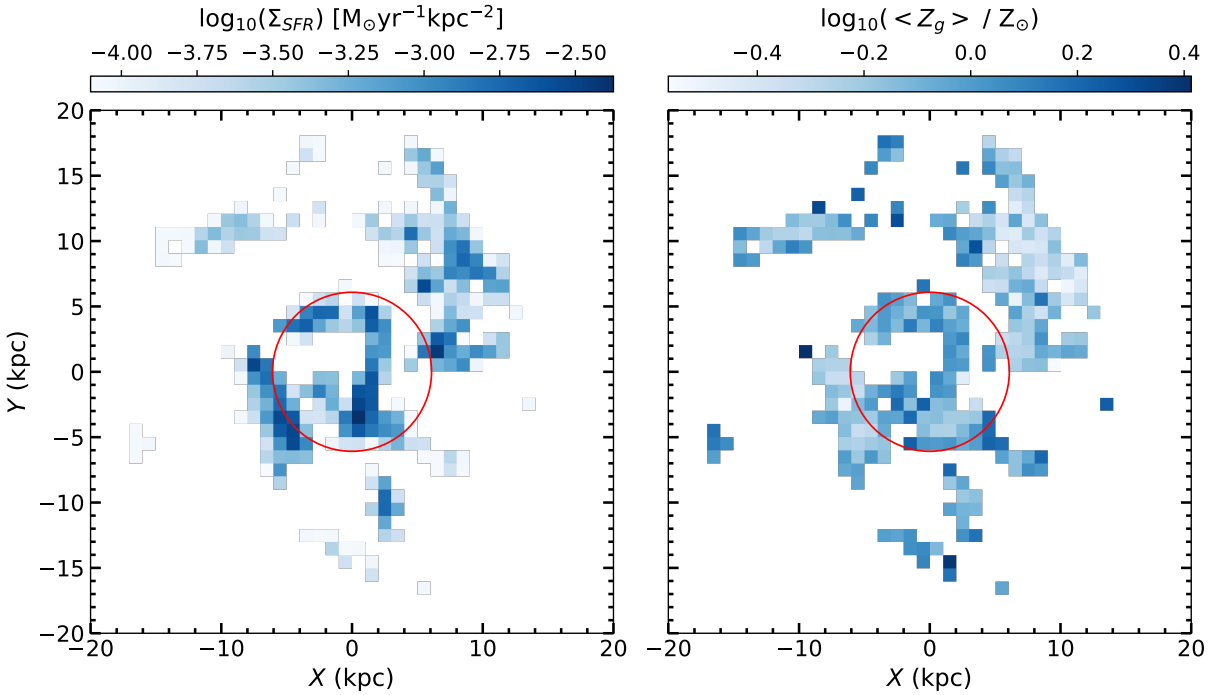

Figure 4.8: Star formation rate surface density (left panel) and mass-weighted average metallicity (right panel) for galaxy 1174755 with $\log_{10}(M_*/M_\odot) = 8.84$. The red circle has a radius equal to the physical radius of a sphere that encloses half of the stellar mass of the galaxy. Note the obvious anti-correlation between the SFR surface density (left panel) and the metallicity (right panel).

The slopes obtained for the EAGLE galaxies show a trend with the stellar mass similar to the one observed by Sánchez-Menguiano et al. (2019), as we see that galaxies with lower masses have negative correlations and galaxies with higher masses positive ones. However, the slope has a higher deviation from the observations in the higher mass bin, which might be due to our lack of statistic in the high-mass end, as there are only five galaxies in this bin.

The regions of high SFR and low metallicites that we see in the disc galaxies of the simulation (e.g. Figures 4.6-4.8) are consistent with an scenario that has already been proposed in the literature (Sánchez Almeida et al., 2018; Sánchez-Menguiano et al., 2019) in which metal-poor accreted gas triggers the star formation in some regions while diluting the previously existing gas and decreasing the mean metallicity of the pre-existing gas.

Therefore, this scenario allows us to explain the local anti-correlation found in star-forming dwarf galaxies in the Local Universe (Sánchez Almeida et al., 2018) and in low-mass nearby spiral galaxies (Sánchez-Menguiano et al., 2019). In contrast, Sánchez-Menguiano et al. (2019) argue that in higher mass galaxies the fraction of more metal-rich pre-existing gas might be relatively higher, and hence having a positive correlation between Z_g and SFR. Thus, those two scenarios would be compatible with the trend of the slope of the local $Z_g - \Sigma_{SFR}$ with the stellar mass shown in Figure 4.9.

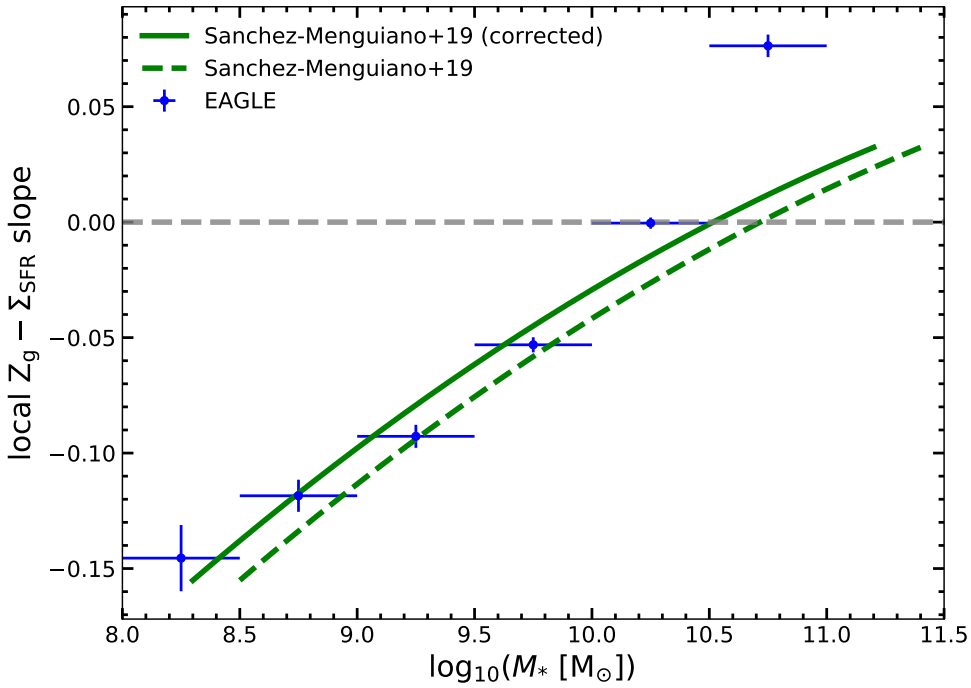

Figure 4.9: Local $Z_g - \Sigma_{SFR}$ slope as a function of galaxy stellar mass. Negative slope means that Z_g decreases when the SFR surface density increases, and vice-versa. The slopes are computed for the subsample of 107 centrals with 'disc-like' features and the galaxies are divided in 6 equally log-spaced stellar mass bins of 0.5 dex. For each bin, the blue point correspond to the slope of a linear fit of the mass-weighted average metallicity as a function of star formation rate surface density of the star-forming gas of all the galaxies that fall in the mass bin. The green dashed line corresponds to the mean slopes observed by Sánchez-Menguiano et al. (2019) in a sample of 736 MaNGA galaxies. The line represents a 2nd order polynomial fit to the actual data. The solid line is the same polynomial shifted in mass to account for the difference in initial mass functions used in MaNGA and EAGLE. The grey dashed line is included for reference.

Moreover, Hwang et al. (2019) analyzed a sample of nearby star-forming late-type galaxies and found that the incidence rate of regions with anomalously low metallicites regions are higher in lower mass galaxies and in the outer regions of the disks, which is also in agreement with EAGLE simulations.

Chapter 5

Conclusions

We have studied the interplay between gas and star formation in galaxies using the state-of-the-art cosmological hydrodynamical simulation EAGLE. In this sense, we assessed the source of the gas that fuels recent star formation in 417 simulated, central galaxies at $z = 0$ with $10^8 < M_* \ [\mathrm{M}_\odot] \leq 10^{11}$, and 338 centrals at $z = 2.01$ with $10^8 < M_* \ [\mathrm{M}_\odot] \leq 10^{10.5}$. For that purpose, we traced back in time the gas that formed new stars in the galaxies at redshift z to find where the gas was at z_{prev} ($z < z_{prev}$), and carried out this analysis for galaxies at two different epochs, $z = 0$ and $z = 2.01$. We identified as new stars the ones formed between z_{prev} and z. For galaxies at $z = 0$, the stars are formed between $z = 0.1$ and $z = 0$ (i.e., stars with ages shorter than 1.34 Gyr), whereas for galaxies at $z = 2.01$, new stars are formed between $z = 3.02$ and $z = 2.01$ (i.e., stars with ages shorter than 1.13 Gyr). We made a classification according to the location of this gas at z_{prev} and distinguish five different categories: 1. the gas that was already bound to the galaxy at the previous redshift; 2. the gas that was not bound to any galaxy at the previous redshift; 3. the gas bound to a galaxy that produced a minor merger; 4. the gas bound to a galaxy that produced a major merger; 5. the gas bound to a 'dark' galaxy that merged (for a summary of the different categories, see Table 3.3). Our findings can be summarised as follows:

- For a given galaxy mass at $z = 0$, the contribution to the initial mass of new stars from stars formed from gas that was already in the galaxy is substantially higher than the one from stars formed from accreted gas, although the importance of major mergers increases at the high-mass end (left panel of Figure 4.1). In contrast, although stars formed from pre-existing gas are still dominant at $z = 2.01$, accreted gas contributes significantly more than at later times, with more than 10% of the new stars forming from gas that was not bound to any galaxy, and with roughly 10% forming from gas accreted through mergers with 'dark' galaxies. Minor and major mergers contribute more with increasing galaxy mass at $z = 2.01$. The dependece with stellar mass is smoother than at $z = 0$ for stars formed from accreted gas (right panel of Figure 4.1).

- New stars formed from gas that was already in the galaxy are the major contributors to the stellar masses of the galaxies at $z = 0$, counting for about 10% of the galaxy mass, except for higher mass galaxies where this contribution decreases to less than a 2%. Nevertheless, we see that in low-mass galaxies, star formation from accreted gas make a

larger contribution to the galaxy mass than in higher mass galaxies. Indeed, for some low-mass objects a large fraction of galaxy mass is produced from accreted gas, given the large dispersion around the median of the distribution (left panel of Figure 4.3). Whereas at high redshift, the mass of new stars formed from pre-existing gas correspond to roughly half of the galaxy stellar mass. Nonetheless, in intermediate- and high-mass objects star formation from accreted gas corresponds to larger mass fractions than at $z = 0$. The variation of the fractions with stellar mass is also smoother (right panel of Figure 4.3).

• At $z = 0$, the stars formed from pre-existing gas and the star-forming gas have quite similar metallicites over the whole mass range. Conversely, the metallicity of the stars formed from gas accreted in mergers with 'dark' galaxies is considerably lower and seems to anti-correlate with the galaxy mass. Minor mergers also contribute with lower metallicities, although the metallicity of this accreted gas is relatively higher at the low- and high-mass ends. New stars in low- and high-mass galaxies formed from major mergers and pre-existing gas have similar metallicites. However intermediate-mass galaxies have an irregular behaviour, but we cannot conclude much due to the lack of merger statistics (Figure 4.5).

• A fraction of the gas classified as unbound gas at $z = 0$ may come from galactic fountains, as the stars formed from this gas have noticeably high metallicities. In this way, although hot galactic winds are operationally classified as not graviationally bound, this ejected gas can cool in the halo and be re-accreted onto the galaxy disc to form stars (Figure 4.5).

• The main mode of accretion at earlier times and in low-mass galaxies at later times is expected to be cold gas accretion. In this sense, there are low-mass EAGLE galaxies at $z = 0$ with a significant contribution of metal-poor gas coming from mergers with 'dark' galaxies, whereas at high redshift this contribution does not vary significantly with galaxy mass. Furthermore, most of the galaxies have contributions from mergers with 'dark' galaxies at earlier times (Figure 3.3).

We also analyzed the local relation between gas-phase metallicity and star formation rate in a subsample of 107 central galaxies at $z = 0$ that have 'disk-like' features. Our morphological selection follows the approach of previous works in the literature, that have characterized the morphologies of EAGLE galaxies constraining their kinematic properties (Correa et al., 2017) and shape parameters (Thob et al., 2019). We generated spatially resolved maps of projected mass-weighted average gas-phase metallicity and star formation rate density of the star-forming gas in the galaxies. For the projection we set the galaxies in a face-on configuration and computed these quantities in kpc^2 bins. In this work, we showed the maps of representative galaxies with different masses. We find that:

• For a high-mass galaxy, there are outskirt regions with higher SFR and lower Z_g, however this relation reverses sign in the central parts of the galaxy (Figure 4.6). For a galaxy with lower mass, we see a more significant anti-correlation between Z_g and Σ_{SFR} in the outer parts of the galaxy than for the higher mass galaxy (Figure 4.7). While Z_g and Σ_{SFR} are prominently more anti-correlated for a galaxy at the low-mass end (Figure 4.8).

We employed these maps of Z_g and Σ_{SFR} to characterize in EAGLE the local relation between gas-phase metallicity and star formation rate that has already been seen observationally in discs of nearby star-forming galaxies (Sánchez Almeida et al., 2018; Hwang et al., 2019; Sánchez-Menguiano et al., 2019). We separated the subsample in log-spaced stellar mass bins of 0.5 dex and for a given bin, we fitted the scatter plot of mass-weighted average metallicity versus star formation rate surface density (which has the contribution of all the galaxies that fall in the bin) to a linear relation. We also compared these findings from EAGLE to the observed local $Z_g - \Sigma_{SFR}$ relation found by Sánchez-Menguiano et al. (2019) for 736 nearby spiral galaxies from the MaNGA survey. This analysis shows that:

- The trend with stellar mass of the slopes of the linear fits from EAGLE galaxies is similar to the one observed by Sánchez-Menguiano et al. (2019). Low-mass galaxies have negative slopes and hence, an anti-correlation between Z_g and Σ_{SFR}, whereas for galaxies at the high-mass end the slope reverses sign and thus, having a positive correlation (Figure 4.9). Nevertheless, we note that there is a considerable deviation from observations at the high-mass end, which may be owing to our lack of statistic in this mass regime.

- The local $Z_g - \Sigma_{SFR}$ anti-correlation present in disc galaxies from EAGLE is consistent with a scenario in which metal-poor gas accretion triggers star formation locally, while diluting the pre-existing gas and decreasing its mean metallicity. This picture has already been proposed in the literature to explain observed regions with high SFR and low metallicities in nearby low-mass galaxies (Sánchez Almeida et al., 2018; Sánchez-Menguiano et al., 2019). Conversely, in the case of higher mass galaxies, Sánchez-Menguiano et al. (2019) suggest that a higher fraction of more metal-rich pre-existing gas might account for the observed positive $Z_g - \Sigma_{SFR}$ correlation, which is also present in EAGLE.

5.1 Future work

One of the main limitations of the analysis carried out in the first part of the project is the lack of statistic at low redshift. Thus, the new generation of hydrodynamical simulations with larger cosmological volumes will provide more statistics, while having sufficient resolution to perform our analysis in low-mass objects. On the other hand, we fixed the evolution time-scale in our analysis to be about 1 Gyr. While this is comparable with the dynamical time of massive galaxies, it cannot account for several dynamical times for dwarf galaxies. In this way, it would be possible to adapt this time scale for each stellar mass bin by using simulation outputs with higher frequency. Note that this is not possible with the data in the public database of EAGLE, but it would be feasible because the EAGLE simulations have reduced data outputs at higher frequency.

Regarding the second part of the project, since we found that the observed local relation is also present in EAGLE disc galaxies with similar trends to the observations, more precise results would be obtained by performing an analysis more similar to the observations. For example, generating data cubes and mock spectra from the simulation to obtain the physical quantities needed, being this approach more comparable to the observations. Furthermore, an in-depth analysis of the regions with high SFR and low metallicites of these discs may bring light to the origin of this relation in the simulation.

For instance, analyzing the path of gas that fuels star formation in those regions and looking where it comes from.

Bibliography

Behroozi, P. S., Wechsler, R. H., & Conroy, C. 2013, The Astrophysical Journal, 770, 57, doi: 10.1088/0004-637X/770/1/57

Binney, J., & Tremaine, S. 2008, Galactic Dynamics: Second Edition

Birnboim, Y., & Dekel, A. 2003, MNRAS, 345, 349, doi: 10.1046/j.1365-8711.2003.06955.x

Brooks, A. M., Governato, F., Quinn, T., Brook, C. B., & Wadsley, J. 2009, ApJ, 694, 396, doi: 10.1088/0004-637X/694/1/396

Bundy, K., Bershady, M. A., Law, D. R., et al. 2015, ApJ, 798, 7, doi: 10.1088/0004-637X/798/1/7

Combes, F. 2013, Memorie della Societa Astronomica Italiana Supplement, 25, 45. https://arxiv.org/abs/1210.5124

Correa, C. A., Schaye, J., Clauwens, B., et al. 2017, MNRAS, 472, L45, doi: 10.1093/mnrasl/slx133

Crain, R. A., Schaye, J., Bower, R. G., et al. 2015, MNRAS, 450, 1937, doi: 10.1093/mnras/stv725

Davis, M., Efstathiou, G., Frenk, C. S., & White, S. D. M. 1985, ApJ, 292, 371, doi: 10.1086/163168

De Rossi, M. E., Bower, R. G., Font, A. S., Schaye, J., & Theuns, T. 2017, MNRAS, 472, 3354, doi: 10.1093/mnras/stx2158

Dekel, A., & Birnboim, Y. 2006, MNRAS, 368, 2, doi: 10.1111/j.1365-2966.2006.10145.x

Dekel, A., Birnboim, Y., Engel, G., et al. 2009, Nature, 457, 451, doi: 10.1038/nature07648

Dolag, K., Borgani, S., Murante, G., & Springel, V. 2009, MNRAS, 399, 497, doi: 10.1111/j.1365-2966.2009.15034.x

Dubois, Y., Pichon, C., Welker, C., et al. 2014, MNRAS, 444, 1453, doi: 10.1093/mnras/stu1227

Ellison, S. L., Patton, D. R., Simard, L., & McConnachie, A. W. 2008, ApJ, 672, L107, doi: 10.1086/527296

Furlong, M., Bower, R. G., Theuns, T., et al. 2015, MNRAS, 450, 4486, doi: 10.1093/mnras/stv852

Furlong, M., Bower, R. G., Crain, R. A., et al. 2017, MNRAS, 465, 722, doi: 10.1093/mnras/stw2740

Genel, S., Dekel, A., & Cacciato, M. 2012, MNRAS, 425, 788, doi: 10.1111/j.1365-2966.2012.21652.x

Guo, Qi; White, S., Boylan-Kolchin, M., De Lucia, G., et al. 2011, MNRAS, 413, 101, doi: 10.1111/j.1365-2966.2010.18114.x

Hwang, H.-C., Barrera-Ballesteros, J. K., Heckman, T. M., et al. 2019, ApJ, 872, 144, doi: 10.3847/1538-4357/aaf7a3

Kereš, D., Katz, N., Weinberg, D. H., & Davé, R. 2005, MNRAS, 363, 2, doi: 10.1111/j.1365-2966.2005.09451.x

Kormendy, J. 2013, ed. J. Falcón-Barroso & J. H. Knapen, 1. https://arxiv.org/abs/1311.2609

Lagos, C. d. P., Theuns, T., Schaye, J., et al. 2016, MNRAS, 459, 2632, doi: 10.1093/mnras/stw717

Lara-López, M. A., Cepa, J., Bongiovanni, A., et al. 2010, A&A, 521, L53, doi: 10.1051/0004-6361/201014803

L'Huillier, B., Combes, F., & Semelin, B. 2012, A&A, 544, A68, doi: 10.1051/0004-6361/201117924

Madau, P., & Dickinson, M. 2014, Annual Review of Astronomy and Astrophysics, 52, 415, doi: 10.1146/annurev-astro-081811-125615

Mannucci, F., Cresci, G.; Maiolino, R., Marconi, A., & Gnerucci, A. 2010, MNRAS, 408, 2115, doi: 10.1111/j.1365-2966.2010.17291.x

McAlpine, S., Helly, J. C., Schaller, M., et al. 2016, A&C, 15, 72, doi: 10.1016/j.ascom.2016.02.004

EAGLE Team. 2017. https://arxiv.org/abs/1706.09899

Planck Collaboration, Ade, P. A. R., Aghanim, N., et al. 2014, A&A, 571, A1, doi: 10.1051/0004-6361/201321529

Olmo-García, A., Sánchez Almeida, J., Muñoz-Tuñón, C., et al. 2017, ApJ, 834, 181, doi: 10.3847/1538-4357/834/2/181

Pillepich, A., Springel, V., Nelson, D., et al. 2018, MNRAS, 473, 4077, doi: 10.1093/mnras/stx2656

Renzini, A., & Peng, Y.-j. 2015, ApJ, 801, L29, doi: 10.1088/2041-8205/801/2/L29

Sánchez, S., Pérez, E., Sánchez-Blázquez, P., et al. 2016, RMxAA, 52, 171. https://arxiv.org/abs/1602.01830

Sawala, T., Frenk, C. S., Fattahi, A., et al. 2016, MNRAS, 457, 1931, doi: 10.1093/mnras/stw145

Schaye, J., Crain, R. A., Bower, R. G., et al. 2015, MNRAS, 446, 521, doi: 10.1093/mnras/stu2058

Silk, J., & Mamon, G. A. 2012, Res. Astron. Astrophys., 12, 917, doi: 10.1088/1674-4527/12/8/004

Springel, V. 2005, MNRAS, 364, 1105–1134, doi: 10.1111/j.1365-2966.2005.09655.x

Springel, V., White, S. D. M., Tormen, G., & Kauffmann, G. 2001, MNRAS, 328, 726, doi: 10.1046/j.1365-8711.2001.04912.x

Sánchez Almeida, J. 2017, in Astrophysics and Space Science Library, Vol. 430, Gas Accretion and Star Formation Rates, ed. A. F. . R. Davé, 67, doi: 10.1007/978-3-319-52512-9_4

Sánchez Almeida, J., Caon, N., Muñoz-Tuñón, C., Filho, M., & Cerviño, M. 2018, MNRAS, 476, 4765, doi: 10.1093/mnras/sty510

Sánchez Almeida, J., & Dalla Vecchia, C. 2018, ApJ, 859, 109, doi: 10.3847/1538-4357/aac086

Sánchez Almeida, J., Elmegreen, B. G., Muñoz-Tuñón, C., & Elmegreen, D. M. 2014, Astron. Astrophys. Rev., 22, 71, doi: 10.1007/s00159-014-0071-1

Sánchez Almeida, J., Muñoz-Tuñón, C., Elmegreen, D. M., Elmegreen, B. G., & Méndez-Abreu, J. 2013, ApJ, 767, 15, doi: 10.1088/0004-637X/767/1/74

Sánchez Almeida, J., Elmegreen, B. G., Muñoz-Tuñón, C., et al. 2015, ApJ, 810, L15, doi: 10.1088/2041-8205/810/2/L15

Sánchez-Menguiano, L., Sánchez Almeida, J., Muñoz-Tuñón, C., et al. 2019, ApJ, 882, 9, doi: 10.3847/1538-4357/ab3044

Thob, A. C. R., Crain, R. A., McCarthy, I. G., et al. 2019, MNRAS, 485, 972, doi: 10.1093/mnras/stz448

Trayford, J. W., & Schaye, J. 2019, MNRAS, 485, 5715, doi: 10.1093/mnras/stz757

Trayford, J. W., Theuns, T., Bower, R. G., et al. 2015, MNRAS, 452, 2879, doi: 10.1093/mnras/stv1461

van de Voort, F., & Schaye, J. 2012, MNRAS, 423, 2991, doi: 10.1111/j.1365-2966.2012.20949.x

van de Voort, F., Schaye, J., Booth, C. M., Haas, M. R., & Dalla Vecchia, C. 2011, MNRAS, 414, 2458, doi: 10.1111/j.1365-2966.2011.18565.x

Vogelsberger, M., Marinacci, F., Torrey, P., & Puchwein, E. 2020, Nat. Rev. Phys., 2, 44, doi: 10.1038/s42254-019-0127-2

Wang, J., Navarro, J. F., Frenk, C. S., et al. 2011, MNRAS, 413, 1373, doi: 10.1111/j.1365-2966.2011.18220.x

Wang, L., Dutton, A. A., Stinson, G. S., et al. 2015, MNRAS, 454, 83, doi: 10.1093/mnras/stv1937

Wetzel, A. R., Hopkins, P. F., Kim, J.-h., et al. 2016, The Astrophysical Journal Letters, 827, L23, doi: 10.3847/2041-8205/827/2/L23